The Astrophysical Journal, 940:65 (17pp), 2022 November 20

https://doi.org/10.3847/1538-4357/ac97e5

© 2022. The Author(s). Published by the American Astronomical Society.

OPEN ACCESS

CrossMark

Collimation of the Relativistic Jet in the Quasar 3C 273

Hiroki Okino[1,2], Kazunori Akiyama[3,4,5], Keiichi Asada[6], José L. Gómez[7], Kazuhiro Hada[5,8], Mareki Honma[5,8,1], Thomas P. Krichbaum[9], Motoki Kino[10,5], Hiroshi Nagai[2,8], Uwe Bach[9], Lindy Blackburn[11,4], Katherine L. Bouman[12], Andrew Chael[13,30], Geoffrey B. Crew[3], Sheperd S. Doeleman[11,4], Vincent L. Fish[3], Ciriaco Goddi[16,14,15,17], Sara Issaoun[11,30], Michael D. Johnson[11,4], Svetlana Jorstad[18], Shoko Koyama[19,6], Colin J. Lonsdale[3], Ru-Sen Lu[20,21,9], Ivan Martí-Vidal[22,23], Lynn D. Matthews[3], Yosuke Mizuno[29], Kotaro Moriyama[24,5], Masanori Nakamura[25,6], Hung-Yi Pu[26], Eduardo Ros[9], Tuomas Savolainen[27,28,9], Fumie Tazaki[5], Jan Wagner[9], Maciek Wielgus[9], and Anton Zensus[9]

[1] Department of Astronomy, Graduate School of Science, The University of Tokyo, 7-3-1 Hongo, Bunkyo-ku, Tokyo 113-0033, Japan; h.okino@grad.nao.ac.jp
[2] National Astronomical Observatory of Japan, 2-21-1 Osawa, Mitaka, Tokyo 181-8588, Japan
[3] Massachusetts Institute of Technology Haystack Observatory, 99 Millstone Road, Westford, MA 01886, USA
[4] Black Hole Initiative, Harvard University, 20 Garden Street, Cambridge, MA 02138, USA
[5] Mizusawa VLBI Observatory, National Astronomical Observatory of Japan, 2-12 Hoshigaoka, Mizusawa, Oshu, Iwate 023-0861, Japan
[6] Institute of Astronomy and Astrophysics, Academia Sinica, 11F of Astronomy–Mathematics Building, AS/NTU No. 1, Sec. 4, Roosevelt Rd, Taipei 10617, Taiwan, R.O.C.
[7] Instituto de Astrofísica de Andalucía-CSIC, Glorieta de la Astronomía s/n, E-18008 Granada, Spain
[8] Department of Statistical Science, The Graduate University for Advanced Studies (SOKENDAI), 10-3 Midori-cho, Tachikawa, Tokyo 190-8562, Japan
[9] Max-Planck-Institut für Radioastronomie, Auf dem Hügel 69, D-53121 Bonn, Germany
[10] Kogakuin University of Technology & Engineering, Academic Support Center, 2665-1 Nakano, Hachioji, Tokyo 192-0015, Japan
[11] Center for Astrophysics | Harvard & Smithsonian, 60 Garden Street, Cambridge, MA 02138, USA
[12] California Institute of Technology, 1200 East California Boulevard, Pasadena, CA 91125, USA
[13] Princeton Gravity Intiative, Jadwin Hall, Princeton University, Princeton, NJ 08544, USA
[14] Dipartimento di Fisica, Universit degli Studi di Cagliari, SP Monserrato-Sestu km 0.7, I-09042 Monserrato, Italy
[15] INAF—Osservatorio Astronomico di Cagliari, via della Scienza 5, I-09047 Selargius (CA), Italy
[16] Universidade de São Paulo, Instituto de Astronomia, Geofísica e Ciências Atmosféricas, Departamento de Astronomia, São Paulo, SP 05508-090, Brazil
[17] INFN, Sezione di Cagliari, Cittadella Univ., I-09042 Monserrato (CA), Italy
[18] Institute for Astrophysical Research, Boston University, 725 Commonwealth Avenue, Boston, MA 02215, USA
[19] Niigata University, 8050 Ikarashi 2-no-cho, Nishi-ku, Niigata 950-2181, Japan
[20] Shanghai Astronomical Observatory, Chinese Academy of Sciences, 80 Nandan Road, Shanghai 200030, People's Republic of China
[21] Key Laboratory of Radio Astronomy, Chinese Academy of Sciences, Nanjing 210008, People's Republic of China
[22] Departament d'Astronomia i Astrofísica, Universitat de València, C. Dr.Moliner 50, E-46100 Burjassot, Spain
[23] Observatori Astronòmic, Universitat de València, C. Catedrático Beltrán 2, E-46980 Paterna, Spain
[24] Institut für Theoretische Physik, Goethe-Universität Frankfurt, Max-von-Laue-Straße 1, D-60438 Frankfurt am Main, Germany
[25] National Institute of Technology, Hachinohe College, 16-1 Uwanotai, Tamonoki, Hachinohe City, Aomori 039-1192, Japan
[26] Department of Physics, National Taiwan Normal University, No. 88, Sec. 4, Tingzhou Rd., Taipei 116, Taiwan, R.O.C.
[27] Aalto University Department of Electronics and Nanoengineering, PL 15500, FI-00076 Aalto, Finland
[28] Aalto University Metsähovi Radio Observatory, Metsähovintie 114, FI-02540 Kylmälä, Finland
[29] Tsung-Dao Lee Institute and School of Physics and Astronomy, Shanghai Jiao Tong University, 800 Dongchuan Road, Shanghai, 200240, People's Republic of China

Abstract

The collimation of relativistic jets launched from the vicinity of supermassive black holes (SMBHs) at the centers of active galactic nuclei (AGNs) is one of the key questions to understand the nature of AGN jets. However, little is known about the detailed jet structure for AGN like quasars since very high angular resolutions are required to resolve these objects. We present very long baseline interferometry (VLBI) observations of the archetypical quasar 3C 273 at 86 GHz, performed with the Global Millimeter VLBI Array, for the first time including the Atacama Large Millimeter/submillimeter Array. Our observations achieve a high angular resolution down to $\sim 60\,\mu$as, resolving the innermost part of the jet ever on scales of $\sim 10^5$ Schwarzschild radii. Our observations, including close-in-time High Sensitivity Array observations of 3C 273 at 15, 22, and 43 GHz, suggest that the inner jet collimates parabolically, while the outer jet expands conically, similar to jets from other nearby low-luminosity AGNs. We discovered the jet collimation break around 10^7 Schwarzschild radii, providing the first compelling evidence for structural transition in a quasar jet. The location of the collimation break for 3C 273 is farther downstream from the sphere of gravitational influence (SGI) from the central SMBH. With the results for other AGN jets, our results show that the end of the collimation zone in AGN jets is governed not only by the SGI of the SMBH but also by the more diverse properties of the central nuclei.

Unified Astronomy Thesaurus concepts: Active galactic nuclei (2035); Blazars (164); Quasars (1319); Relativistic jets (1390); Very long baseline interferometry (1769)

1. Introduction

Relativistic jets ejected from active galactic nuclei (AGNs) are tightly collimated plasma outflows from galactic centers, known as the most energetic persistent phenomena in the universe. Their formation, acceleration, and collimation mechanisms constitute one of the most important questions in

AGN jet physics (e.g., reviewed in Blandford et al. 2019). In particular, jet collimation processes have been studied by focusing on jet structures since they provide various information not only about the jet itself but also about their surrounding environment contributing to jet confinement (Begelman & Li 1994; Komissarov et al. 2007, 2009; Fromm et al. 2018).

The detailed nature of the jet collimation can be addressed by high-angular-resolution observations using very long baseline interferometry (VLBI; e.g., Boccardi et al. 2017; Hada 2019), allowing direct comparisons with special or general relativistic (SR or GR) magnetohydrodynamic simulations (Chael et al. 2018; Nakamura et al. 2018; Fromm et al. 2019). In particular, intensive studies of the M87 jet in the last decade have provided new insights about jet collimation since that jet is the best source for investigating the global jet structures from the immediate vicinity of the central black hole (BH) to beyond the host galaxy (Asada & Nakamura 2012; Hada et al. 2013, 2016; Nakamura & Asada 2013; Kim et al. 2018; Walker et al. 2018; Event Horizon Telescope Collaboration et al. 2019a; Park et al. 2019a). Following the aforementioned pioneering works on M87, jet shapes have been measured mainly from several nearby sources: NGC 6251 (Tseng et al. 2016), NGC 4261 (Nakahara et al. 2018), 1H 0323+342 (Hada et al. 2018), Cygnus A (Boccardi et al. 2016; Nakahara et al. 2019), NGC 1052 (Nakahara et al. 2020; Baczko et al. 2022), NGC 315 (Boccardi et al. 2021; Park et al. 2021), 3C 84 (Nagai et al. 2014; Giovannini et al. 2018), and for a large number of jet samples collected by the long-term monitoring MOJAVE program[31] (Pushkarev et al. 2017). More recently, Kovalev et al. (2020) investigated jet widths from over 300 sources and found the transitions of jet shapes from 10 nearby sources. They also found that the range of the transition locations is $\sim 10^{5-6}$ gravitational radii from the core, which may indicate a common property of nearby AGN jets.

The collimation properties of distant quasars are still unclear due to the difficulties in resolving the transverse jet shape. Indeed, Algaba et al. (2017) systematically measured core sizes for distant radio-loud AGNs to investigate the upstream jet structures. However, the core size is often unresolved even at an extremely high angular resolution with a space radio dish (e.g., Gómez et al. 2016), and is often measured with high systematic uncertainties resulting from the limited angular resolution. Although the jet structure of the flat-spectrum radio quasar (FSRQ) 4C 38.41 was measured by Algaba et al. (2019), they could not detect significant collimation breaks because of the limited range of the measured jet scales. In addition, the physical parameters for this source, such as the BH mass and the jet viewing angle, have large uncertainties. Therefore, to understand the jet collimation for high-powered AGN like quasars, observations with a high angular resolution for the well-studied sources at other wavelengths are required to transversely resolve the detailed structures down to the bases of the jets.

In this paper, we study the quasar 3C 273 (1226+023), well known as one of the brightest extragalactic objects and the closest quasars (Schmidt 1963) with prominent jets (Davis et al. 1985; Conway et al. 1993; Bahcall et al. 1995; Jester et al. 2005; Perley & Meisenheimer 2017). The 3C 273 jets have been observed many times since their discovery because the elongated jet is a unique target for resolving down to the central (sub)parsec scale with VLBI observations (Krichbaum et al.

1990; Lobanov & Zensus 2001; Savolainen et al. 2006; Kovalev et al. 2016; Bruni et al. 2017, 2021; Jorstad et al. 2017; Lister et al. 2019, 2021). Furthermore, recent infrared interferometric observations with the GRAVITY instrument on the Very Large Telescope Interferometer (Gravity Collaboration et al. 2017) precisely estimated the BH mass and viewing angle for 3C 273 as $M_{\rm BH} = (2.6 \pm 1.1) \times 10^8 \, M_\odot$ and $\theta = 12° \pm 2°$ (Gravity Collaboration et al. 2018).[32] The estimated BH mass yields a linear angular relation of 1 mas ~ 2.7 pc $\sim 1.2 \times 10^5 \, R_{\rm s}$, which makes 3C 273 one of the best-resolved quasars. For these reasons, 3C 273 is the ideal target for investigating the global structure of a quasar jet. For 3C 273, a preliminary detection of the transition from the parabolic to conical shape has been reported in an early work of a subset of the authors in a conference proceeding (Akiyama et al. 2018), based on a marginal detection of a parabolic jet from single-band data sets at 43 GHz only covering a narrow range of the spatial area. It also lacks a careful consideration of frequency-dependent locations of radio cores at different frequencies due to the effect of synchrotron self-absorption relevant for the innermost jet probed at millimeter wavelengths. The presence of the transition has remained inconclusive in the earlier work.

In this paper, we report new multifrequency observations of the jet of the quasar 3C 273 observed with several global VLBI networks. In particular, the Global Millimeter VLBI Array (GMVA) at 3.5 mm/86 GHz including the phased Atacama Large Millimeter/submillimeter Array (ALMA; Matthews et al. 2018) provided a strong advantage, remarkably increasing the north–south resolution and sensitivity (see also Issaoun et al. 2019 for the first published image with GMVA+ALMA on Sgr A*). These observations provided us with high-fidelity imaging of the finest jet structure of 3C 273 from the innermost subparsec scale region with a maximum resolution of several tens of microarcseconds (μas).

The paper is organized as follows. In Section 2, we describe the observations and data reduction. Images were reconstructed with the state-of-the-art regularized maximum likelihood methods as described in Section 3, and further analyzed in Section 4. We show the global jet structure of 3C 273, including the core shift measurements and the jet collimation profile in Section 5. The physical implications of our observations are discussed in Section 6. Finally, we summarize our results in Section 7. In this paper, we assume a flat ΛCDM cosmology (e.g., Planck Collaboration et al. 2014) with $H_0 = 70 \, {\rm km \, s^{-1} \, Mpc^{-1}}$, $\Omega_{\rm M} = 0.3$, and $\Omega_\Lambda = 0.7$, and we adopt values of $M_{\rm BH} = 2.6 \times 10^8 \, M_\odot$ and a viewing angle of $\theta = 9°$[33] for the 3C 273 jet.

2. Observations and Data Analysis

2.1. GMVA 86 GHz

We observed 3C 273 with the GMVA at 86 GHz ($\lambda \sim 3.5$ mm) on 2017 April 3 (project code MA008), as one of the first

---

[31] https://www.physics.purdue.edu/MOJAVE/index.html

[32] Li et al. (2022) reported a new estimation of BH mass of $\sim 10^9 \, M_\odot$ and viewing angle of $\sim 5°$ for 3C 273 during the review process of our paper. These new estimates are based on a joint analysis of spectroastrometric data in Gravity Collaboration et al. (2018) and new data from reverberation mapping with a more generalized model. We confirm that these estimates do not affect our main results and conclusions.

[33] Previous studies have reported various values for the viewing angle of the 3C 273 jet. Jorstad et al. (2017) reported $\theta \sim 6°$ from VLBI monitoring at 43 GHz. Meyer et al. (2016) showed the possible range of 3°.8–7°.2. However, other studies have reported larger values of $\theta \gtrsim 10°$ (Savolainen et al. 2006; Gravity Collaboration et al. 2018). Therefore, we assume $\theta = 9°$, which is broadly consistent with previously reported values of jet viewing angles.

Table 1
Summary of Observations of 3C 273

Array	Project Code	Stations (1)	Frequency (GHz) (2)	Obs. Date (yyyy/mm/dd) (3)	Beam Size (mas × mas, deg) (4)	Geometric Mean (mas) (5)
VLBA	BH151	VLBA(10)	1.667	2008/02/02	$10.312 \times 4.460, -4.3$	6.778
HSA	BA122	EB+VLBA(10)	15.368	2017/03/26	$1.025 \times 0.408, -6.3$	0.647
HSA	BA122	EB+VLBA(10)	23.768	2017/03/26	$0.577 \times 0.273, -3.1$	0.397
HSA	BA122	EB+VLBA(10)	43.168	2017/03/26	$0.325 \times 0.128, -6.1$	0.204
GMVA	MA008	AA+EB+ON+PV+YS+VLBA(8)	86.268	2017/04/03	$0.061 \times 0.052, -42.7$	0.057

Note. (1) The stations that participated in the observations. The two-letter codes for each station are as follows: ALMA (AA), Effelsberg (EB), Onsala (ON), Pico Veleta (PV), Yebes (YS), Brewster (BR), Fort Davis (FD), Hancock (HN), Kitt Peak (KP), Los Alamos (LA), Maunakea (MK), North Liberty (NL), Owens Valley (OV), Pie Town (PT), and St. Croix (SC). Ten VLBA stations (BR, FD, HN, KP, LA, MK, NL, OV, PT, and SC) are included in VLBA(10), and eight stations, excluding HN and SC, in VLBA(8). (2) The observed central frequency. (3) The observing date. (4) Sizes of the major/minor axes and position angles of the synthesized beam with uniform weighting. (5) The beam size of an equivalent circular Gaussian with the same beam solid angle derived from the geometric mean of the major- and minor-axis beam sizes.

VLBI observations with ALMA (see Goddi et al. 2019, for a detailed description). The phased ALMA, eight VLBA stations, and four European stations participated in our observation, as summarized in Table 1. 3C 273 and calibrators (3C 279) were observed for a track of ∼16 hr, almost a full track for the given observing array. ALMA participated for ∼5.2 hr in the middle of the track, providing baselines to both VLBA and European stations. Data were recorded at a total bandwidth of 256 MHz per polarization, which was further subdivided into four 58 MHz intermediate frequencies (IFs) of 116 channels each.

Data were correlated using the DiFX correlator (Deller et al. 2011) at the Max Planck Institute for Radio Astronomy in Bonn, Germany. We note that Maunakea (MK) did not provide robust fringe detections on any of the observed sources because of the bad weather at MK throughout the GMVA campaign during spring 2017 (see also Issaoun et al. 2019). We also note that the visibility phases of PV baselines at each subband IF had an instrumental offset of $180°$ in subsequent channels of 32 MHz widths owing to a misconfiguration of the subband alignment in the correlation stage.

Initial data calibration was performed using the Astronomical Image Processing System (AIPS; Greisen 2003). Preceding standard calibration, the inner-IF phase offsets in the PV baselines were corrected using a manually created bandpass table. Visibility amplitudes were a priori calibrated in the standard manner; visibilities at each baseline were first normalized with the available autocorrelation spectra and then scaled with the system-equivalent flux densities of the corresponding stations.

Phases were calibrated in a standard manner with multiple fringe-fitting runs after parallactic angle correction. First, the instrumental phases stable across the track, such as phase bandpass, inter-IF phase, and delay offsets, were corrected with a scan of 3C 273, providing strong detection to all stations except MK. This enabled coherent integration across the entire bandwidth and more sensitive fringe-fitting by combining all IFs. Second, the delay and rate offsets of each scan were calibrated at the solution interval of the scan length, which is typically several minutes. Then, short-timescale phase rotations were fringe-fitted at solution intervals of 10 s.

The new addition of ALMA to GMVA has significantly improved the overall array performance. Figure 1 shows the uv coverage for our GMVA observation of 3C 273. The long baselines beyond ∼1.5 Gλ in north–south (N–S) direction correspond to ALMA. The phased ALMA has improved the
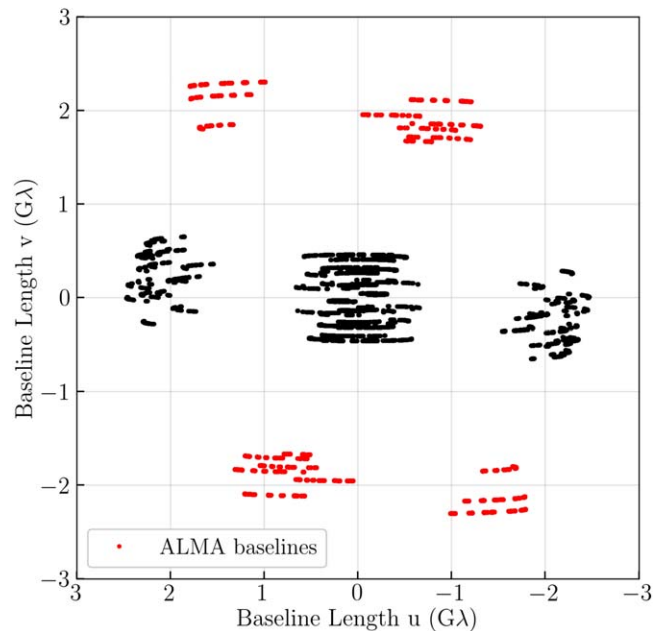

Figure 1. uv coverage of the GMVA observation at 86 GHz. Baselines to ALMA are shown in red. Data are averaged at 60 s.

angular resolution of the GMVA observations in the N–S direction by more than a factor of two (see Section 5.1). Furthermore, ALMA provides detection at very high signal-to-noise ratio on long baselines to both VLBA and European stations at ∼1.5–2.0 Gλ (Figure 2). The sensitive ALMA secured the detection of fringes to most of the stations in the array while it was participating in the observation.

2.2. HSA 15/22/43 GHz

We performed multifrequency observations of 3C 273 at 15, 22, and 43 GHz with the High Sensitivity Array (HSA) on 2017 March 26, eight days before our GMVA observations (project code: BA122). The observing array consisted of the 10 VLBA stations and the 100 m Effelsberg (EB) telescope in Germany, as summarized in Table 1. Full-track observations were performed for ∼11 hr, of which EB participated in the first ∼3.4 hr. Data were recorded at dual circular polarizations with four 64 MHz IFs subdivided into 256 channels, providing
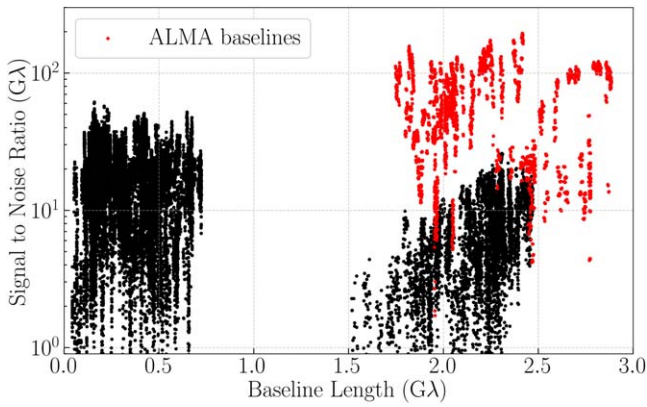
Figure 2. The signal-to-noise ratios of visibilities on 3C 273 as a function of projected baseline length. Data are averaged at 60 s. Baselines to ALMA are shown in red.

an aggregate of 256 MHz per polarization. Data were correlated using the VLBA DiFX correlator.

The initial data calibration for the HSA data was performed using AIPS. We note that the EB baselines in several IFs showed lower visibility amplitudes and larger scattering in visibility phases due to the bandpass issue, which cannot be calibrated in this stage. These data were removed prior to the data calibration. Data were calibrated in a standard manner similar to the GMVA data sets described in Section 2.1; amplitudes were a priori calibrated, and then phases were calibrated with fringe-fitting. Fringes were detected on all stations, and similar baseline coverages were obtained at all three observing frequencies.

2.3. VLBA 1.7 GHz

To complement our data on the larger-scale jet structure, we reduced an archival VLBA 1.7 GHz data set of 3C 273 observed in 2008 February (project code: BH151). The data set has one of the best hour-angle coverage among existing archival data sets at 1.7 GHz.[34] Data were reduced in a standard manner in AIPS. Fringes were detected on all 10 VLBA stations, as summarized in Table 1.

3. Imaging

We reconstructed multifrequency images of 3C 273 from the GMVA, HSA, and VLBA data sets presented in Section 2 with regularized maximum likelihood (RML) methods implemented in SMILI (Akiyama et al. 2017a, 2017b). Our GMVA and HSA arrays are heterogeneous and were expected to have more residual calibration errors at higher frequencies, such as 43 and 86 GHz. Furthermore, our GMVA observations had sparse *uv* coverages lacking intermediate baselines as shown in Figure 1. The traditional iterative hybrid mapping using CLEAN (e.g., Högbom 1974) with self-calibration implemented in popular packages such as AIPS and Difmap (Shepherd 1997) is generally more challenging than for the lower-frequency data sets and does not offer the flexibility. RML methods provide a more flexible imaging framework, by directly using various

types of data sets including robust closure quantities (e.g., Thompson et al. 2017) and a wider range of assumptions for the source images.

We employed an imaging approach inspired by recent Event Horizon Telescope (EHT) imaging of M87 (Event Horizon Telescope Collaboration et al. 2019b) that explored a wide range of parameters, implying assumptions of source images, and assessed uncertainties in images and their deliverables more conservatively. Using a scripted RML imaging pipeline, we explored the distribution of images giving a satisfactory fit to the data, which were all further used in the image analysis in Section 4. We briefly introduce the RML method in Section 3.1. Then, we describe the imaging pipeline used in our imaging of 3C 273 in Section 3.2, and the details of the imaging parameter survey in Section 3.3.

3.1. RML Methods

RML methods are a new class of imaging techniques that were conceived to overcome many of the technical challenges of millimeter VLBI imaging, particularly with the EHT. RML imaging takes a forward-modeling approach inspired by Bayesian statistics, directly solving for an image without using a dirty beam or dirty map. RML methods have been demonstrated to improve the overall quality of image reconstruction not only for synthetic observations (e.g., Honma et al. 2014; Chael et al. 2016, 2018; Akiyama et al. 2017a, 2017b; Kuramochi et al. 2018) but also for actual interferometric measurements with VLBI arrays (e.g., Event Horizon Telescope Collaboration et al. 2019b; Issaoun et al. 2019; Kim et al. 2020; Janssen et al. 2021) and connected interferometers (e.g., Matthews et al. 2018; Yamaguchi et al. 2020).

RML methods derive a reasonable or conservative image from an infinite number of images consistent with given interferometric measurements by solving for an image that minimizes the sum of data consistency metrics, such as χ^2 terms, and regularization functions that mathematically describe prior assumptions for the source morphology. This framework allows a flexible choice of input data, for instance, the direct use of closure quantities free from antenna-based calibration errors (e.g., Chael et al. 2016, 2018; Akiyama et al. 2017b; Blackburn et al. 2020) and further inclusion of various observing effects such as systematic non-closing errors (Event Horizon Telescope Collaboration et al. 2019b). Popular regularization functions include ℓ_1-norm, total variation (TV), and total squared variation (TSV), enforcing sparsity in some basis of the image (Honma et al. 2014; Ikeda et al. 2016; Akiyama et al. 2017a, 2017b; Kuramochi et al. 2018) and the information entropy of the image (e.g., Chael et al. 2016). By combining various regularization functions, RML methods can explore a wide range of images consistent with the data, often leading to reconstruction with more reasonable assumptions of the target source (e.g., Akiyama et al. 2017a, 2017b; Event Horizon Telescope Collaboration et al. 2019b). Further technical and mathematical details of the RML approaches adopted in this study are described in Event Horizon Telescope Collaboration et al. (2019b).

3.2. Imaging Pipeline

We used a scripted pipeline in Python for our RML imaging with SMILI. In the pipeline, 3C 273 images were reconstructed from AIPS-calibrated data (see Section 2) by utilizing

---

[34] We cross-checked archival data of a more close-in-time VLBA observation at 1.6 GHz in 2014 with the experiment code of BG216H. We obtained a jet width profile consistent with the data sets used in this paper, confirming that the width of the 1.6 GHz jet does not change significantly over the timescale of 10 yr.

Table 2
List of Imaging Parameters

Freq. (GHz)	Sys. Error (%)	ℓ_1^w	TV	TSV	MEM	Total No. of Parameters	No. of Top-set Parameters
1.6	0, 1	1	1	$0, 10^{-2}, 10^{-1}, 1, 10$	$0, 10^{-2}, 10^{-1}, 1$	40	15
15	0, 1	$10^{-1}, 1, 10$	1	$0, 10^{-2}, 10^{-1}, 1, 10$	$0, 10^{-2}, 10^{-1}, 1, 10$	150	45
22	0, 1	$10^{-1}, 1, 10$	1	$0, 10^{-2}, 10^{-1}, 1, 10$	$0, 10^{-2}, 10^{-1}, 1, 10$	150	30
43	0, 1	$10^{-1}, 1, 10$	1	$0, 10^{-2}, 10^{-1}, 1, 10$	$0, 10^{-2}, 10^{-1}, 1, 10$	150	35
86	0, 1	$10^{-1}, 1$	1	$0, 10^{-2}, 10^{-1}, 1$	$0, 10^{-2}, 10^{-1}, 1$	64	24

weighted-ℓ_1, TV, TSV, and maximum entropy method (MEM) regularizers (see Appendix A of Event Horizon Telescope Collaboration et al. (2019b) for mathematical definitions). The pixel size of the image is typically set to one-tenth of the mean FWHM size of the uniform-weighted synthesized beam summarized in Table 1. Prior to imaging, the *uv* coordinates of the data were rotated by 45° counterclockwise, resulting in the same rotation of the image-domain axis, and the horizontal axis approximately aligned with the jet direction. This allows us to use a narrower rectangular field of view of the image and minimizes the computational cost of imaging. Then, the visibilities were coherently averaged for 60 s, after manually flagging outliers. If specified, systematic errors were added in quadrature to the thermal noise of the time-averaged complex visibilities to account for non-closing errors. We explored 0 or 1% of non-closing errors within the range expected for polarization leakages (e.g., Zhao et al. 2022).

Our imaging procedure is iterative, with four stages of imaging and self-calibration. In the first stage, the initial image is set to a circular Gaussian with the size corresponding to the geometric mean of the major and minor-axis sizes of the synthesized beam at each observed frequency (see Table 1). The subsequent stages of imaging started with the final image of the previous stage convolved with the above circular Gaussian. The first two stages begin with the initial image and use visibility amplitudes, log closure amplitudes, and closure phases for imaging. At each stage, the visibility amplitudes of all baselines added a 5% error in quadrature to the thermal noise to account for the amplitude calibration uncertainties. In the final two stages, the imaging uses complex visibilities and closure quantities.

3.3. Imaging Parameter Survey

Using the pipeline described in Section 3.2, we explored a wide range of parameters, as summarized in Table 2. At each frequency, the parameter survey examined several tens to a few hundred parameter sets with four to five parameters: potential systematic non-closing errors (denoted as Sys. Error) and the regularization parameters for the ℓ_1^w, TV, TSV, and MEM regularizers. Among the sets of imaging parameters explored, we selected "top sets" of the parameters that provide reconstructed images with reasonable fits to data. The distributions of the corresponding top-set images allow us to assess and identify the morphologies commonly seen and insensitive to the imaging choices as well as their uncertainties among the reconstructed images consistent with our interferometric measurements.

We started imaging with the HSA data at 15 GHz. We adopted the published VLBA image at 15 GHz and Stokes *I* on 2017 May 25 (project code BL229AH) from the MOJAVE program (Lister et al. 2018), which was the closest epoch to our

HSA observations, as the soft mask of the imaging region with ℓ_1^w regularization. This allows noise suppression outside of the area, which has historically had no significant emission.[35] Then, the best-fit image among the top-set 15 GHz images is adopted as the soft mask for subsequent 22 GHz image processing to maximize the consistency between adjacent frequencies. We processed data at higher frequencies (43 and 86 GHz) in the same manner using best-fit images at the adjacent lower frequencies. For *L*-band data, we used the *L*-band VLBA image in Akiyama et al. (2018) as its soft mask.

We selected the top-set images with good fits to the data using χ^2 statistics. For the selection of top-set parameters, we adopted the minimum threshold of 1.5 for the reduced χ^2 values of full complex visibilities, amplitudes, and closure quantities of self-calibrated images. Consequently, 15 to 45 images were selected at each frequency, as summarized in Table 2, and used in post-imaging analysis.

3.4. Total Flux Scaling for GMVA 86 GHz

The overall scaling of visibility amplitudes depends strongly on the accuracy of the a priori calibration of visibility amplitudes based on measurements of the system-equivalent flux density at each station, which often have large systematic errors in high-frequency VLBI observations above ~86 GHz (see, e.g., Koyama et al. 2016; Kim et al. 2018, for previous GMVA observations). We assumed Effelsberg (EB) and Pico Veleta (PV), often considered as reliable stations for a priori calibrations, as the reference stations for overall gain scaling (see, e.g., Angelakis et al. 2015; Fuhrmann et al. 2016; Agudo et al. 2018). We scaled the total flux density of our GMVA 86 GHz images such that the median gain amplitude of EB and PV is unity. The derived scaling factor is ~1.46, and we obtained the scaled total flux (median in the top set) as ~3.1 Jy. The scaling of amplitudes and the total flux density described here will not affect our main results based on the collimation profile measured from the source morphology (Section 4.2). We note that our 86 GHz images show reasonable spectral indices to images at lower frequencies (see Section 5.3).

4. Image Analysis

With all top-set images from the imaging parameter survey (Section 3.3), we investigate the jet profile as a function of distance from the central black hole. First, we identified the position of the central black hole using the core shift effect as described in Section 4.1. Then, the jet radii at each frequency were measured, as described in Section 4.2.

---

[35] The typical jet proper motion of 3C 273 is a few mas yr^{-1}, which does not change the overall jet emission structure in a few months.

4.1. Core Shift Measurements

Core shift is a positional shift of the radio core between two different observing frequencies due to the frequency dependence of the optical depth of the synchrotron self-absorption (Blandford & König 1979). In our study, we employed the widely used self-referencing method (e.g., Lobanov 1998; O'Sullivan & Gabuzda 2009; Pushkarev et al. 2012; Fromm et al. 2013; Hada et al. 2018) to measure the core shift of 3C 273, based on a well-vetted assumption that the emitting regions from the extended jet are optically thin features, and their positions do not change at different frequencies. From this assumption, one can obtain the core offset values between two images at different frequencies after aligning the corresponding optically thin emission regions. We only used the images at 15, 22, 43, and 86 GHz observed within a week (see Table 1). The offsets were measured for four combinations (15/22, 22/43, 43/86, 15/43 GHz).[36] For each frequency pair, we derived the offsets using all combinations of the top-set images and adopted their mean values as the measured offsets.

First, we needed to identify the core position for each jet image to compare them at different frequencies. We decided on the locations of some components in the upstream regions by several circular Gaussian model fittings using Difmap. We applied this analysis to all the top-set images and identified four to seven components for the 15–86 GHz images. We set the core at the most upstream component for each image.

To obtain the core offset between two frequencies, we used a two-dimensional cross-correlation of the optically thin emission regions in the jet images following the widely used method described in Croke & Gabuzda (2008). First, the pixel size of both images was set to a twentieth of the restoring beam size at the lower frequency, which was much smaller than the angular resolution at both frequencies. Next, we convolved both images with the restoring beam at the lower frequency. After masking the optically thick core regions of both images, we computed the cross-correlation coefficient r_{xy} defined by

$$r_{xy} = \frac{\sum_{i=1}^{n}\sum_{j=1}^{n}(I_{\nu 1,ij} - \bar{I}_{\nu 1})(I_{\nu 2,ij} - \bar{I}_{\nu 2})}{\sqrt{\sum_{i=1}^{n}\sum_{j=1}^{n}(I_{\nu 1,ij} - \bar{I}_{\nu 1})^2 \sum_{i=1}^{n}\sum_{j=1}^{n}(I_{\nu 2,ij} - \bar{I}_{\nu 2})^2}} \quad (1)$$

where $I_{\nu,ij}$ is the intensity at pixel (i, j) at frequency ν, and $\bar{I}$ is the averaged intensity in the calculated region. The cross-correlation coefficient r_{xy} is a function of the relative positional offset $(\Delta x, \Delta y)$. The positional shift between two images at frequencies ν_1 and ν_2 is given by the location of the global maximum r_{xy}. The core offset was defined as the remaining positional offset of the peaks after aligning the corresponding optically thin emission regions.

4.2. Jet Profile Measurements

We investigated the jet collimation in 3C 273 using multi-frequency images. Prior to analysis, we cut off the brightness distribution for all the images below the rms values (see Section 5.1) at each frequency to remove the noise outside the jet regions. Then, the jet radius was measured as a function of distance from the core at each frequency in two steps.

First, we measured the position angle (PA) of the jet at each distance from the core. Following Pushkarev et al. (2017), we

took a circular slice of the image centered at the core with a radius corresponding to each distance and adopted the intensity-weighted centroid as the PA of the jet at the corresponding distance.

After deriving the PA, we measured the jet radius at each distance. Because the jet bends on milliarcsecond scales, we examined two ways of slicing the image to measure the jet radius. The first one is to take a slice perpendicular to the PA at each distance, and the other is to slice the image perpendicular to the local tangent line of the PA profile, following Pushkarev et al. (2017). The effective jet radius was measured by taking the second moment σ_w of the cross section along with each slice at each distance. Then, the FWHM of the jet was obtained as FWHM $= 2\sqrt{2\ln 2}\,\sigma_w$. We derived the deconvolved FWHM (w) defined as $w = \sqrt{\text{FWHM}^2 - \theta_{\text{beam}}^2}$, correcting the blurring effects with the restoring beam at the FWHM of θ_{beam}[37] (see Table 1). Finally, the jet radius r at each distance was obtained from half the size of the deconvolved FWHM (i.e., $r = w/2$).

The jet radius profile was measured with an interval of half of the restoring beam size (see Table 1). We only accept measurements of jet radius that satisfy the following three criteria: (i) the FWHM is larger than θ_{beam} so that the vertical jet emission is well resolved, (ii) the distance from the radio core is greater than $2 \times \theta_{\text{beam}}$ to conservatively remove the effect of the unresolved core, and (iii) the peak intensity of the slice is three times larger than the mean of the residual rms noise derived from all top-set images (see Section 5) at each frequency except for 22 GHz. At 22 GHz, instead, the threshold was set to be nine times larger than the mean residual rms noise to make reliable measurements only at bright locations in the sparse intensity distribution (see the image in Figure 5). The jet radius profile at each frequency was measured for all top-set images with the above two slicing methods. Then, the mean and standard deviation of the jet radius at each distance and frequency were adopted as the corresponding jet radius and its uncertainty, respectively.

5. Results

5.1. GMVA Image

In Figure 3, we show the mean total intensity image of the 3C 273 jet with GMVA at 86 GHz derived by averaging all top-set reconstructions (24 images) obtained from the imaging parameter survey in Section 3.3. Here we show the mean image restored at two characteristic resolutions of our GMVA observations equivalent to uniform weighting.[38] Our new image provides the sharpest view of the inner jet at 86 GHz thanks to the critical addition of ALMA. Without ALMA, the corresponding beam sizes will be $265 \times 50\,\mu$as in uniform weighting, providing significantly worse resolutions along the N–S direction by a factor greater than 2.5. The spatial resolution of our observations is also higher than that of previous

---

[36] The other two (i.e., 15/86 and 22/86 GHz) pairs were omitted due to the lack of extended emission commonly seen at both frequencies.

[37] Although interferometric imaging with RML, in principle, does not require a post-imaging beam convolution to obtain piecewise smooth images, the raw image may contain some over-resolved features that are not strongly supported by data. To reduce potential bias from such features, in this work, we adopt the conventional approach that derives deconvolved widths from ones measured from beam-convolved images widely used with CLEAN imaging.

[38] The restoring beam is arbitrary for RML methods, given that the nature of methods is such that the synthesized beam is not used for deconvolution. Data weighting is equivalent to the natural weighting of CLEAN imaging since data are only weighted by thermal noise and not by uv density, while the reconstructed images are known to have a high fidelity at the resolution comparable to, or higher than, uniform weighting.
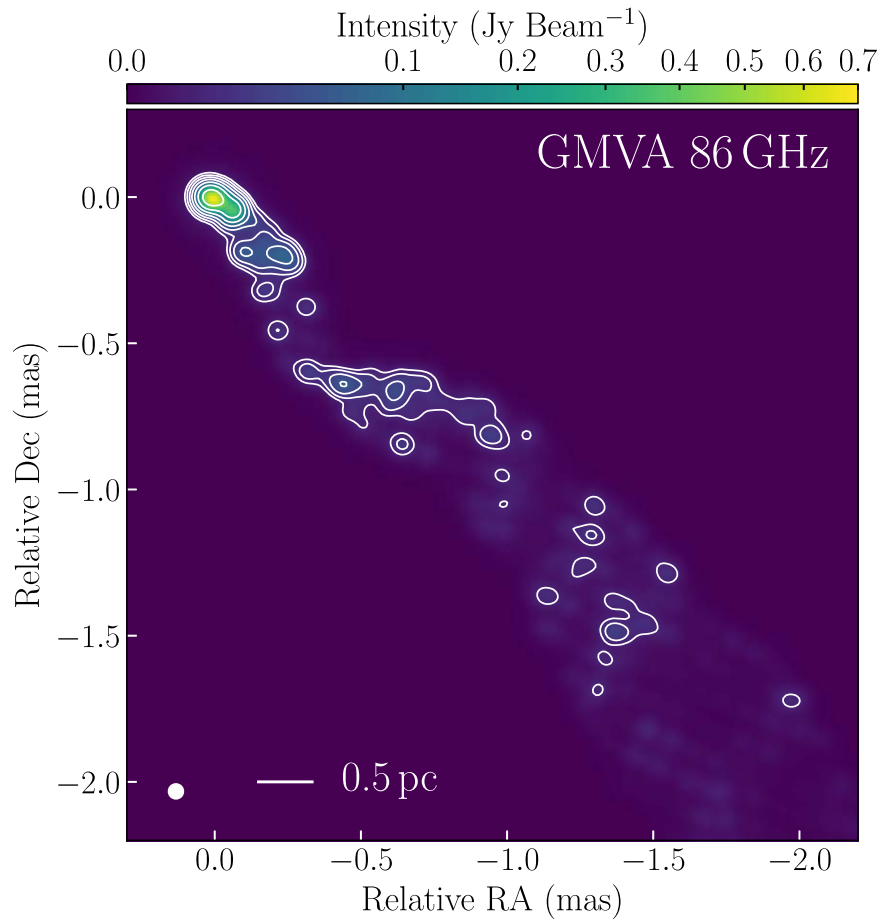
Figure 3. The inner-jet image of 3C 273 obtained with the GMVA observation including ALMA at 86 GHz. Here we show the mean of the top-set reconstructions restored at the resolution with a uniform weighting scheme. The image is restored with a circular beam of 57 μas (indicated in the bottom left corner) corresponding to the geometric mean of the uniform-weighting beam of 61×52 μas. The peak intensity is 0.69 Jy beam^{-1}. The contours are multiplies by factors of 2, from the lowest contour level of 6.5 mJy beam^{-1}.

observations, such as the high-sensitivity VLBA + GBT observations in Hada et al. (2016) with a resolution of 340×110 μas at PA $= -10°$. The high resolution of our new observation allows us to resolve the vertical structure of the inner jet within a few milliarcseconds from the core at 86 GHz for the first time.

To assess the image uncertainty quantitatively, we obtained residual images using the top-set reconstructions (not blurred) as the image models in the Difmap software. We calculated the image rms values for each residual in the top set, and derived the mean value of $\sim$3 mJy beam^{-1} as the representative image uncertainty at 86 GHz with a natural weighting scheme. We then determined the lowest contour level for the uniform-weighting beam to be the same dynamic range ($\sim$100) as the one for natural weighting.

In addition, the final top-set reconstructions have some variations in the image domain depending on the imaging parameters. Figure 4 shows the standard deviation image of GMVA 86 GHz across the top-set reconstructions. The brightest core shows the largest emission ($\sim$200 mJy beam^{-1}), while the faint and extended emissions show smaller variation. These results suggest that the variability in the image domain, especially in the bright region, is dominated by the choice of imaging parameter rather than the rms of the residual images.

The median value of the scaled total flux densities among the top sets of 86 GHz images is $\sim$3.1 Jy (Section 3.4),

corresponding to $\sim$30% of the arcsecond-scale core flux density measured with ALMA in Band 3 during this GMVA campaign (Goddi et al. 2019). The extended jet emission at 3 mm is broadly consistent with the 7 mm jet, implying optically thin spectra (see Section 5.3) and suggesting that the rest of the ALMA core flux density has been resolved out at the shortest VLBI baselines with fringe spacings equivalent to a few milliarcseconds.

5.2. HSA and VLBA Images

In Figure 5, we show lower-frequency images of 3C 273 observed with the HSA and VLBA, which were all averaged over the top-set reconstructions similar to the GMVA images in Figure 3. The overall jet morphology is consistent with previous ground-based (MOJAVE: Lister et al. 2018; VLBA-BU-Blazar[39]: Jorstad et al. 2017) and space-based VLBI observations (Radio Astron: Bruni et al. 2017, 2021). Regardless of the observing frequency, the 3C 273 jet extends in the southwest direction with multiple bright knots whose relative locations are consistent between different frequencies.

The HSA 43 GHz image shows the inner jet structure within $\sim$2 mas, and two extended components around 4 and 7 mas from the core. These overall morphology is consistent with a
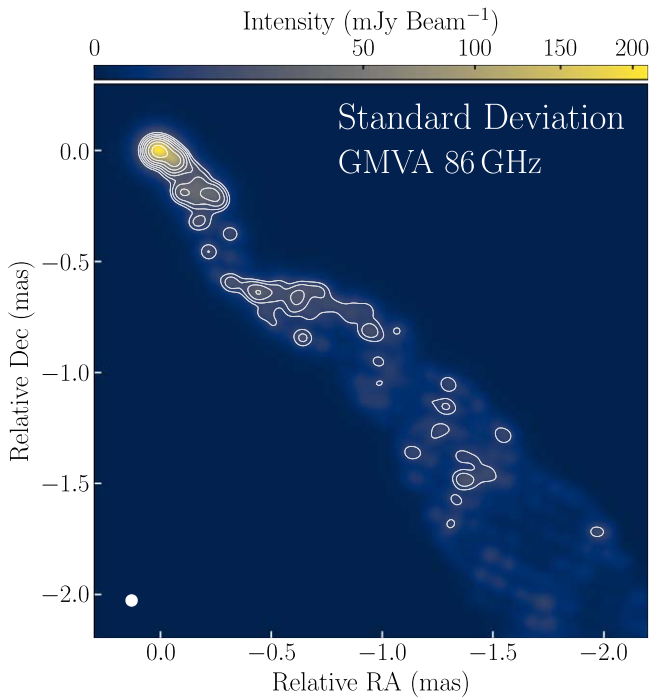
---

[39] http://www.bu.edu/blazars/VLBAproject.html

Figure 4. Standard deviation of the top-set reconstructions of GMVA 86 GHz restored with the circular Gaussian beam of 57 μas shown by the white circle in the bottom left corner. The contours represent the mean image shown in Figure 3.

close-in-time image in the database of the VLBA-BU-Blazar program observed a week previously (2017 March 19).

The HSA 15 and 22 GHz images show the same regions with a bright core and extended jet emissions up to ~25 mas from the core. One can see that the direction of the jet changes at ~10 mas from the core, with the PA changing from ~$-140°$ (upstream) to ~$-120°$ (downstream). In the jet, several components are located at the same position at both frequencies. However, the faint jet component is not detected at 22 GHz unlike at 15 GHz, due to the optically thin synchrotron emission from the jet (see Section 5.3) and also the limited uv coverage for short baselines at 22 GHz compared with 15 GHz.

In our VLBA 1.7 GHz image, the jet emissions downstream of ~20 mas are reconstructed with our imaging. The image is similar to the 3C 273 jet shown in Kovalev et al. (2016) at the same frequency band. One can see the bright component at ~40 mas and the extended jet emission at ~100 mas from the core.

5.3. Spectral Index Maps

We measured the spectral index (defined α as $I_\nu \propto \nu^\alpha$) of the jet emission between two adjacent frequency bands. To derive the spectral index map for each pair of images, we first aligned the two images by adopting the offset determined by the two-dimensional cross-correlation (see Section 4.1). Then, the spectral index maps were derived for all possible pairs of top-set images at two frequencies. Then, we averaged over all spectral index maps for each frequency pair to create the mean spectral index map.

In Figure 6, we show the mean spectral index map of the 3C 273 jet for each pair of neighboring frequency bands. In all frequency pairs, the 3C 273 jet consistently shows spectra that

are optically thick upstream of the core, become flat near the core, and then become optically thin downstream. These features are commonly observed in radio jet sources (e.g., Hovatta et al. 2014), therefore suggesting that the core offsets derived in Section 4.1 are plausible.

5.4. Core Shift

In Table 3, we show the measured core offsets for each pair of frequencies. The measured offsets are in the x-direction, parallel to the large-scale jet axis. The standard deviations of the measured offsets are the same or less than the pixel sizes of the regridded images used for these measurements. Therefore, the measured offsets do not depend on the different combinations of imaging parameter sets used to reconstruct the top-set images.

We fit a power-law model of the core shift caused by the synchrotron self-absorption of the jet emission (e.g., Lobanov 1998). We assume that the core location at the frequency ν_i relative to the 86 GHz core is given by

$$\Delta x_i = A_x(\nu_i^{-k} - \nu_{86}^{-k}), \qquad (2)$$

$$\Delta y_i = A_y(\nu_i^{-k} - \nu_{86}^{-k}), \qquad (3)$$

for each direction, where $\nu_{86} = 86.3$ GHz. The power-law index k depends on the optically thin spectral index of the synchrotron emission, magnetic field, and particle density distributions. Assuming a conical jet with a constant velocity and in the equipartition state between magnetic and particle energy densities, $k \approx 1$ has been shown from the synchrotron self-absorption model proposed by Blandford & Königl (1979), which was confirmed in many sources by previous core shift measurements (see also Pushkarev et al. 2012, and references therein). For 3C 273, Lisakov et al. (2017) has performed multiepoch core shift measurements and reported values of k close to 1 for each epoch. Therefore, given the small sets of frequency pairs available in the presented observations, we assume $k = 1$ and only derive coefficients (A_x, A_y) in our analysis.

In this model, the positional offsets (μ_x, μ_y) of the radio cores between each frequency pair (ν_i, ν_j) are described as

$$\mu_x = \Delta x_i - \Delta x_j = A_x(\nu_i^{-k} - \nu_j^{-k}), \qquad (4)$$

$$\mu_y = \Delta y_i - \Delta y_j = A_y(\nu_i^{-k} - \nu_j^{-k}). \qquad (5)$$

We derive the best-fit model parameters by comparing the model offsets above with measured ones through the least-squares fitting based on χ^2 defined by

$$\chi^2 = \sum_{(i,j)} \left\{ \frac{A_x(\nu_i^{-k} - \nu_j^{-k}) - \mu_x}{\sigma_x} \right\}^2$$

$$+ \sum_{(i,j)} \left\{ \frac{A_y(\nu_i^{-k} - \nu_j^{-k}) - \mu_y}{\sigma_y} \right\}^2. \qquad (6)$$

We found the best-fit parameters of $A_x = -5.635 \pm 2.424$ and $A_y = 0.278 \pm 2.424$, which minimize χ^2. The errors here indicate a 68.3% confidence interval derived from the χ^2 surface. With these values, Equations (2) and (3) can be used to derive the location of the upstream end of the jet, often considered the black hole position (e.g., Hada et al. 2011), by
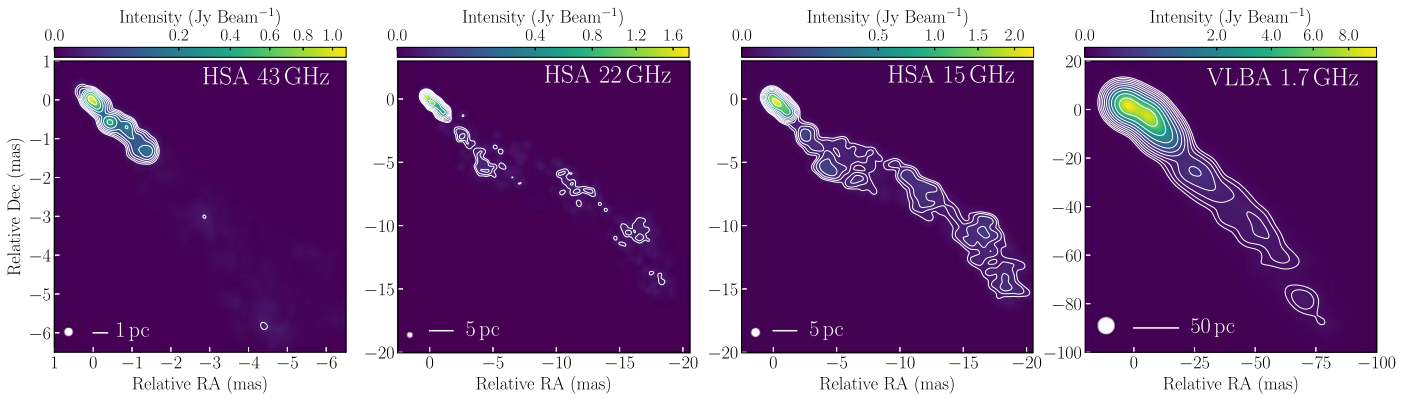
Figure 5. Multifrequency images of 3C 273 jets with the HSA at 43, 22, and 15 GHz and the VLBA at 1.7 GHz. Each panel shows the mean top-set image at each frequency restored by the circular Gaussian beam with the beam solid angle of the uniform-weighting beam size in Table 1. The lowest contour levels are 6.5 mJy beam^{-1} at 43 GHz, 8.2 mJy beam^{-1} at 22 GHz, 7.1 mJy beam^{-1} at 15 GHz, and 11.6 mJy beam^{-1} at 1.7 GHz. The contours for all images are multiplied by a factor of 2. The lowest contour level of each image is estimated from the mean residual image rms of the top-set reconstructions.

taking $\nu_i \to \infty$. From the best-fit parameters, we obtained the location of the jet apex at $x_0 = 65\,\mu$as and $y_0 = -3\,\mu$as upstream[40] of the 86 GHz core for 3C 273. Figure 7 shows the resultant core positions along the large-scale jet axis (i.e., x-direction). The lower-frequency core is located at a greater distance from the central black hole, as anticipated for the core shift caused by synchrotron self-absorption (Blandford & Königl 1979; Lobanov 1998).

5.5. Jet Collimation Profile of 3C 273

Figure 8 shows the radius and position angle profile of the 3C 273 jet as a function of the deprojected distance from the central black hole. Our VLBI measurements cover deprojected distances ranging from $\sim 10^5\,R_s$ to $\sim 10^8\,R_s$. The radius profile at each frequency smoothly connects. Near $z \sim 10^7\,R_s$, the jet radius profile shows a sharp increase by a factor of ~ 2, where the PA of the jet sharply changes by $\sim 20°$ to the north. The overall PA profile meanders around the mean PA of $-138°$, coinciding with the large-scale jet (Conway et al. 1993).

The jet radius profile in the outer region beyond $\sim 10^7\,R_s$ is steeper than that in the inner region. Thus, we fit the power-law functions to the jet radius profile to quantify the jet shape in each region. The details of our model selection are described in the Appendix.

Here, we excluded the region from $4 \times 10^6\,R_s$ to $10^7\,R_s$ (the gray shaded region in Figure 8) from our fitting analysis because of its peculiar and complex morphologies not seen in the rest of the jet. In Figure 9, we show the streamline of the jet image of HSA 15 GHz to illustrate the region that we excluded from our fitting analysis. This region shows a rapid swing in the streamline from the global position angle, and simultaneously the vertical profiles of the jet show highly asymmetric ridge-like structures not seen in the rest of the global jet. These peculiar morphologies make it difficult to define and measure the width of the jet in a consistent way with the rest of the global jet.

First, we model the jet radius $r(z)$ with a couple of single power-law functions ($r(z) \propto z^a$), separately fitting to each of the upstream ($z < 4 \times 10^6\,R_s$) and downstream ($z > 10^7\,R_s$)

regions. The best-fit values and associated uncertainties of the parameters are estimated using the percentile bootstrap method, where in each trial the parameters are derived by applying an unweighted least-squares method to the data sets randomly resampled from the original data, allowing duplication. After 10,000 bootstrap trials, we adopt the median values as the best-fit parameters, and one-third of the 99.7% percentile confidence intervals as their 1σ uncertainties. The power-law index is found to be $a = 1.28^{+0.08}_{-0.05}$, indicating a conical/hyperbolic shape in the downstream region, whereas $a = 0.66^{+0.04}_{-0.05}$ is indicative of parabolic collimation found in the upstream region.

Furthermore, we also examine a joint fitting of both regions with a broken power-law function defined by

$$r(z) = R_0\, 2^{(a_u - a_d)/2} \left[1 + \left(\frac{z}{z_b}\right)^s\right]^{(a_u - a_d)/2} \quad (7)$$

following Nakahara et al. (2018). R_0 is the scale factor, z_b is the location of the break, and a_u and a_d are the power-law indices of the upstream and downstream regions, respectively. Here s is the parameter controlling the sharpness of the curvature at the transition point, which is fixed to be $s = 10$. The best-fit parameters and their errors are derived using the bootstrapping method in the same manner. The power-law indices in the downstream and upstream regions are found to be $a_d = 1.31^{+0.10}_{-0.06}$ and $a_u = 0.67^{+0.02}_{-0.04}$, respectively, which are both consistent with the results of the above double power-law fitting. The jet shape transition is found to occur at $z_b = 1.1^{+0.1}_{-0.2} \times 10^7\,R_s$. These results show that the 3C 273 jet has a transition in its shape from semiparabolic to conical/hyperbolic at the deprojected distance of $\sim 10^7\,R_s$ from the central black hole.

6. Discussion

6.1. Nature of the Jet Collimation in 3C 273

Our new quasi-simultaneous observations clearly show the transition of the jet shape from semiparabolic to conical/hyperbolic at $\sim 10^7\,R_s$ from the central black hole, providing the first compelling example of a collimation break in a quasar jet. Interestingly, the transitional location roughly coincides with the region at $\sim 4 \times 10^6$ to $10^7\,R_s$ where the jet width ($2r$)

---

[40] The location of the jet apex was derived for $k = 1$, and may vary by at most a factor of two in the range $k \sim 0.8$–1.2 constrained by Lisakov et al. (2017). These uncertainties do not affect the main conclusions of this paper.
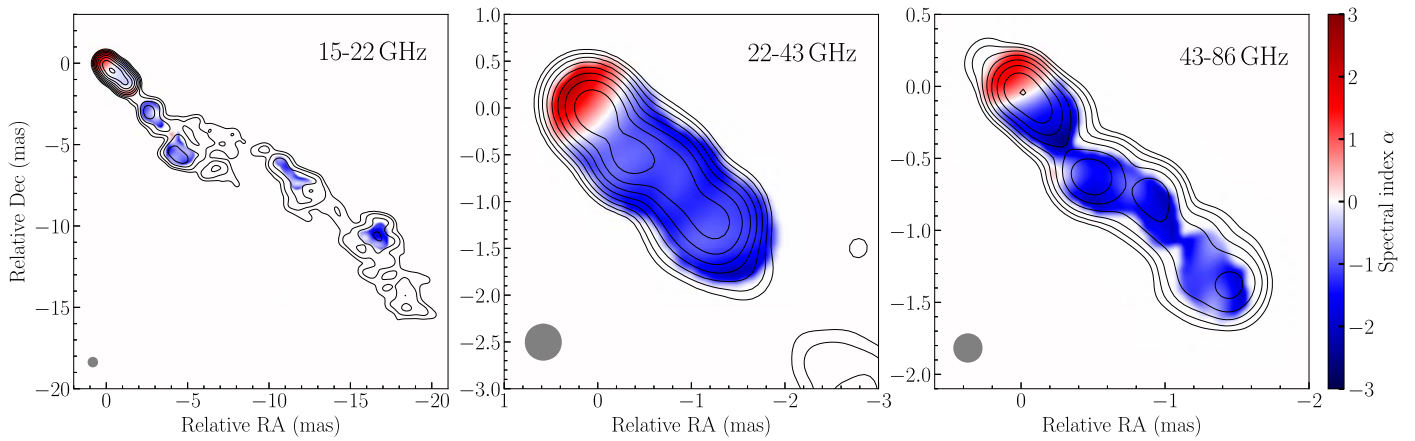
Figure 6. Spectral index maps between pairs of neighboring frequencies labeled in the top right corner of each panel. Spectral index α is defined by $I_\nu \propto \nu^\alpha$. Spectral index values in each pair were calculated from all images in the top sets of both frequencies after aligning the images using cross-correlation (Section 4.1) and averaging them. The contours in each panel represent the mean image of the lower frequency of the HSA as shown in Figure 5.

Table 3
Positional Offsets of the Core between Different Frequencies

ν_1, ν_2 (GHz) (1)	N (2)	Pixel (mas) (3)	μ_x (mas) (4)	μ_y (mas) (5)	σ_x (mas) (6)	σ_y (mas) (7)
15.4, 23.7	1350	0.032	0.000	0.036	0.032	0.032
23.8, 43.2	1050	0.020	−0.224	0.005	0.020	0.020
15.4, 43.2	1575	0.032	−0.129	0.032	0.032	0.032
43.2, 86.3	840	0.010	−0.077	−0.010	0.010	0.010

Note. (1) Frequency pairs. (2) Total number of combinations. (3) Pixel size of regridded images used to measure offsets. (4) Mean offset in the x-direction. (5) Mean offset in the y-direction. (6) Standard deviation of the offsets in the x-direction. (7) Standard deviation of the offsets in the y-direction.

rapidly expands by a factor of $\sim$2 with significant bending, which was not used in the fitting because of its peculiarity (see Figure 9). Recent space-based VLBI observations with Radio Astron at 1.6 GHz revealed the complicated limb-brightened jet emission in this area (Bruni et al. 2021). Mertens & Lobanov (2015) shows non-ballistic motions of jet components along the northern and southern limbs over 14 years, which is longer than the jet crossing time of this region considering the typical proper motion of the jet ($\sim$1 mas yr^{-1}, Lister et al. 2019). After passing through the location of the collimation break, the northern and southern limbs smoothly merge into a single limb, and its position angle farther downstream is temporally and spatially stable over 26 years of 15 GHz observations of the MOJAVE program.[41] The stability of the broadened, double-ridge structure, apparently around the collimation break, suggests a stationary magnetohydrodynamic feature, possibly triggered by some changes in the circumjet environment causing pressure mismatch with the jet (e.g., Mizuno et al. 2015), as the HST-1 knot in M87 near the collimation break is indicated to be (Asada & Nakamura 2012).

The jet velocity field is another important physical quantity that is closely related to jet collimation. This prediction is supported by various VLBI observations of M87 (Nakamura & Asada 2013; Asada et al. 2014; Park et al. 2019b, 2021) and

---
[41] http://www.physics.purdue.edu/astro/MOJAVE/sourcepages/1226+023.shtml
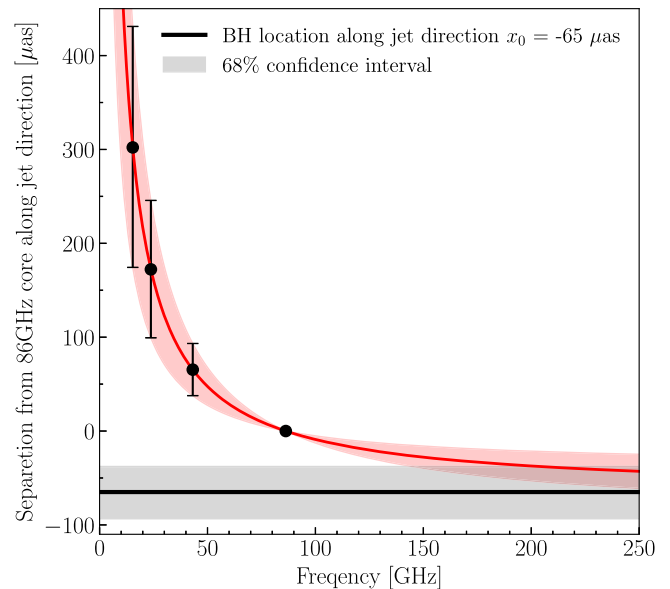
Figure 7. The core position along the large-scale jet axis as a function of the frequency based on the fitted power-law model. The core positions, denoted by the black dots, are relative to the 86 GHz core. The red line shows the best-fit power-law model, and the black line shows the best-fit location of the central black hole. The error bars of the best-fit core positions and the shaded area of the best-fit model indicate the 68% confidence interval estimated from the χ^2 surface of the fitted parameters (Section 5.4).

1H 0323+342 (Hada et al. 2018), and statistical studies of large samples of AGN jets (Homan et al. 2015). In Figure 10, we show the profile of the apparent jet velocities of 3C 273 from long-term monitoring observations at 15 GHz by the MOJAVE program (Lister et al. 2019) and at 43 GHz by the BU-Blazar program (Jorstad et al. 2017), compared to the collimation profile. Except for the stationary knot features at $\lesssim$1 mas identified in the literature (Savolainen et al. 2006; Jorstad et al. 2005, 2017; Bruni et al. 2017; Lisakov et al. 2017), Figure 10 indicates that the jet has already been accelerated to relativistic speed with an apparent velocity of at least $\sim$5c before the collimation break. This trend in the 3C 273 jet differs from that of M87, which shows gradual accelerations in the parabolic regions and velocity saturation at the collimation break (Asada
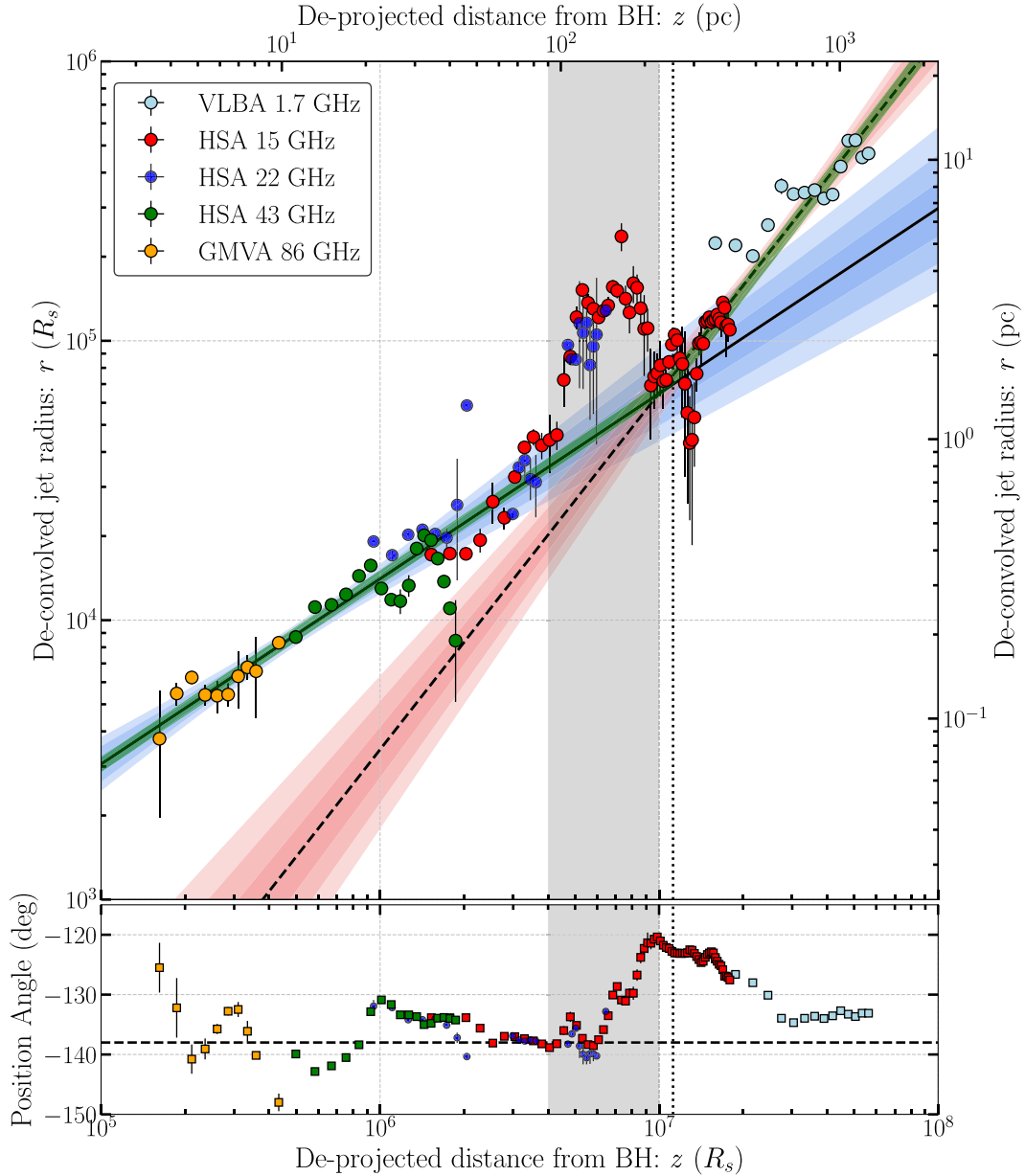
Figure 8. The radius and PA of the 3C 273 jet as a function of the deprojected distance from the central black hole. The deprojected distance from the central black hole is derived using the best-fit core shift model at a viewing angle of $i = 9°$ (see Section 1) for the black hole mass of $M_{BH} = 2.6 \times 10^8 M_\odot$ (Gravity Collaboration et al. 2018). Upper panel: the jet radius profile. The colored circles and associated error bars indicate the mean values and standard deviations of the measurements, respectively. Different colors show measurements from different observations, as shown in the legend. The solid and dashed lines show single power-law fits ($r \propto z^a$) to the inner side, semiparabolic ($a = 0.66$), and to the outer side, conical/hyperbolic ($a = 1.28$), respectively. The surrounding shaded areas represent the uncertainty of the single power-law fits (1σ, 2σ, 3σ). The green line represents the best-fit broken power-law function, giving the best-fit distance of the jet shape break of $z_b = 1.1 \times 10^7 R_s$ shown on the vertical dotted line. Lower panel: the jet PA profile. The color convention is the same as in the upper panel. The horizontal dashed line shows PA = $-138°$, which is broadly consistent with the axis of the large-scale jet (e.g., Davis et al. 1985; Conway et al. 1993). The gray shade across both panels shows the region excluded from the fitting analysis because of a large bending seen in the jet (see the details in Section 5.5).

et al. 2014; Park et al. 2019a). Further observations of the jet kinematics in both the inner (<1 mas) and outer (>10 mas) regions would be useful for investigating the detailed velocity field in the collimation zone of 3C 273 and would provide useful comparisons to radio galaxies.

For the innermost jet at the inner subparsec scale, one can compare our results with recent submilliarcsecond-scale observations with near-infrared optical interferometry. 3C 273 has been intensively studied with the Very Large Telescope Interferometer, which recently resolved the broad-line regions (BLRs) with a size of 46 μas ~ 0.1 pc as an ionized gas disk

(Gravity Collaboration et al. 2018), and the dust torus emission with a size of ~ 150 μas ~ 0.4 pc (Gravity Collaboration et al. 2020). The innermost collimation profile of the 3C 273 jets, expected by extrapolating to a farther inner region, is smaller than the measured geometry of the resolved BLRs and hot dust torus distributions. Such a region, where the jet is surrounded by the BLRs and dust torus, would be reachable with future higher-frequency observations, such as with the EHT at 230 or 345 GHz. Future higher-frequency VLBI observations will be critical for understanding the role of such an external medium, which is common in quasars in jet collimation.
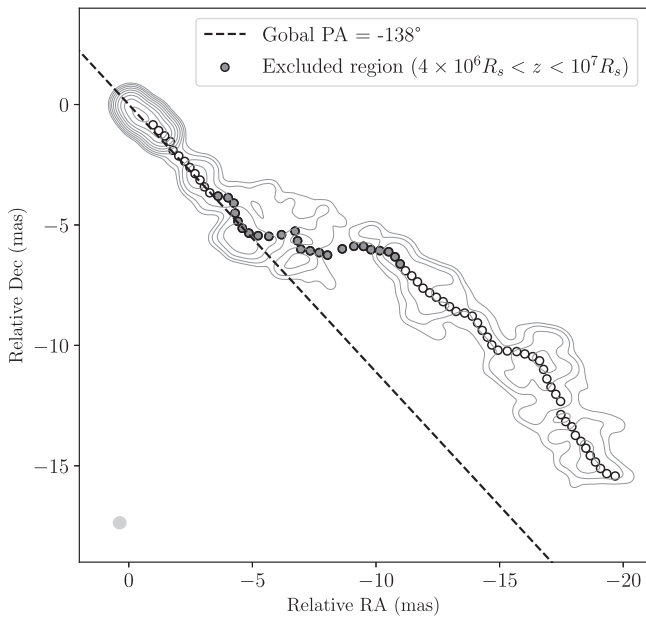
Figure 9. One of the top-set images from HSA 15 GHz observation (gray contours) overlaid with the streamline of the 3C 273 jet (filled and open circles). The regions excluded from our fitting are indicated by gray filled circles, showing a stable complex and bending double-ridge-like morphology not seen in the rest of the global jet (see Section 6.1). A black dashed line indicates the global position angle of the jet estimated from the large-scale jet image (e.g., Davis et al. 1985).
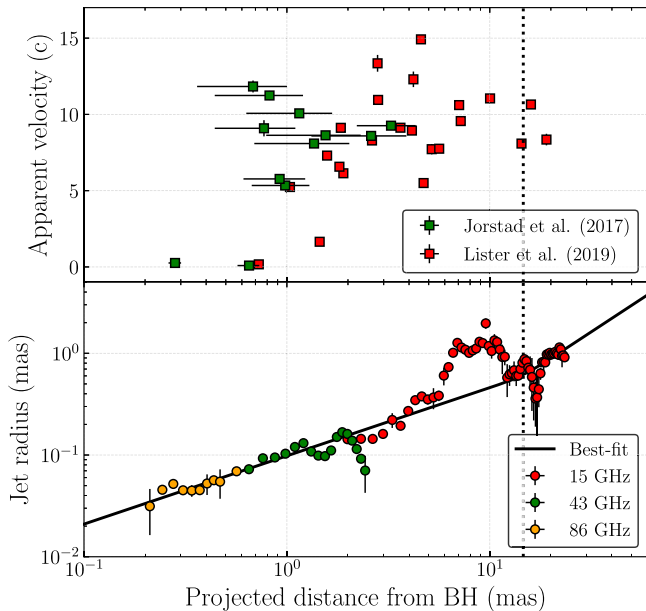

Figure 10. The apparent velocity (top) and collimation profile (bottom) as functions of the projected distance from the black hole. The black dotted line represents the best-fit location of the collimation break.

Downstream of the collimation break, the jet structure up to about the kiloparsec scale shows a conical/hyperbolic expansion with a power-law index of $a = 1.28$. The unconfined structures downstream of the jets have been found in other AGN jets (Pushkarev et al. 2017; Kovalev et al. 2020). To investigate the jet shape beyond the VLBI scales ($\gtrsim 1$ kpc), we show additional measurements based on CLEAN images from MERLIN and Very Large Array (VLA) observations at 1.6 GHz and 5 GHz from Akiyama et al. (2018) and Perley &
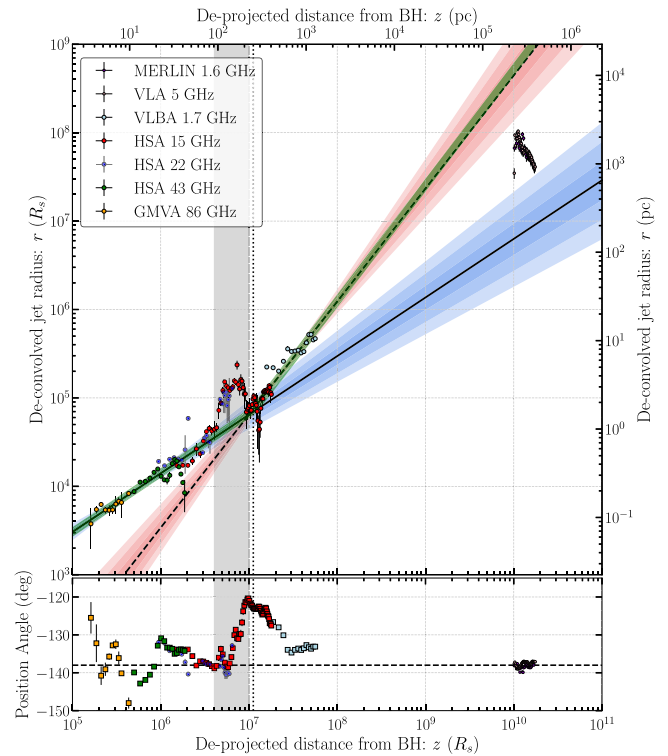
Figure 11. The jet radius and PA profiles of the 3C 273 jet, extended from Figure 8 to include measurements of the large-scale jet beyond the deprojected distance of $\sim$200 kpc traced with VLA 5 GHz and MERLIN 1.6 GHz.

Meisenheimer (2017), respectively, in Figure 11. These additional measurements are obtained from the kiloparsec-scale radio lobe at the terminal end of the 3C 273 jet. Although previous observations detected the intermediate-scale ($\sim 1''$–$10''$) jet emission between the central core and the kiloparsec-scale lobe (e.g., Perley & Meisenheimer 2017), the transverse structure is not well resolved, and the radius cannot be measured reliably. This causes a lack of measurements at 10^8–$10^{10} R_s$. The inner semiparabolic line, if extrapolated, significantly underestimates the jet radius at the kiloparsec scale. On the other hand, the jet radius at this scale is smaller than the extrapolated conical/hyperbolic line, and these kiloparsec-scale jets can be more conically connected to 1.7 GHz measurements. Future observations of the intermediate scale would be useful for constraining the propagation of the jet into the kiloparsec-scale radio lobe and for investigating detailed jet features interacting with the ambient ionized/molecular gas (Husemann et al. 2019) and hot gas cocoons (Bromberg et al. 2011).

6.2. Comparison with Other AGN Sources

The jet structure has been investigated for many objects in recent decades, and the transitions of jet collimation profiles have been discovered in several jets of radio galaxies and BL Lac objects. The presented results on 3C 273 have added the case of a quasar jet. To compare our 3C 273 results with other AGN jets, we show in Figure 12 the relation between the black hole mass and the deprojected distance of the jet collimation break for both 3C 273 and other AGN sources. The break locations are widely distributed from $\sim 10^4 R_s$ to $\sim 10^8 R_s$, where 3C 273 is located on the further side.

A popular interpretation for the origin of the jet collimation break is that the transition of the external pressure profile
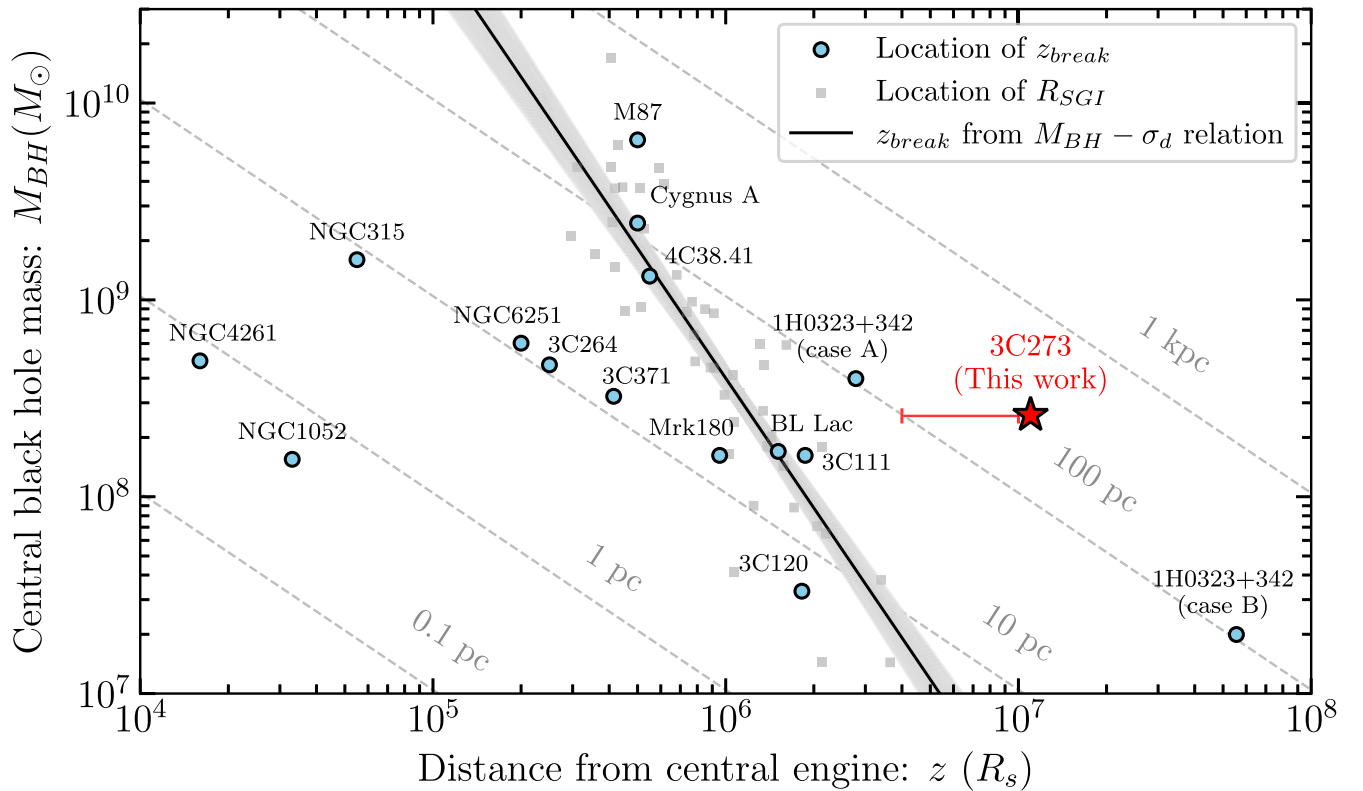
Figure 12. The relation between the black hole mass and the deprojected distance of the jet collimation break from the central engine. The red star shows our results from the 3C 273 jet, and the cyan circles show results from other sources reported in the literature. The red horizontal bar indicates the region of a persistent feature seen near the break distance with a complex bending double-ridge-like morphology potentially associated with the transition in the jet shape (see Figure 9 and Section 6.1). To compare with the location of the SGI, we show the SGI locations of the classical bulges and elliptical galaxies in gray squares taken from Kormendy & Ho (2013). The black solid line and gray shaded area are the best-fit model and the 1σ error range of the relation between the black hole mass and SGI location, transformed from the M_{BH}–σ_d relation in Kormendy & Ho (2013). The dotted lines show the actual distances in parsecs. The results of other sources are obtained from the following references; M87: Asada & Nakamura (2012), NGC 6251: Tseng et al. (2016), NGC 4261: Nakahara et al. (2018), Cygnus A: Nakahara et al. (2019), NGC 1052: Nakahara et al. (2020), NGC 315: Park et al. (2021), 4C 38.41: Algaba et al. (2019), 3C 264: Boccardi et al. (2019), 1H 0323+342: Hada et al. (2018), and other sources: Kovalev et al. (2020). Note that we show two cases of different black hole masses for 1H 0323+342 (see Section 6.2).

triggers the end of the jet collimation, where the external pressure does not provide enough support to confine the jet (e.g., Asada & Nakamura 2012; Tseng et al. 2016). For the pioneering case of M87, Asada & Nakamura (2012) discussed that the transition of the jet shape may result from the transitional change in the external pressure profile of the circumjet medium near the Bondi radius and the end of the sphere of gravitational influence (SGI). This interpretation is motivated by X-ray observations, which indicate that the different pressure profiles of the ambient gas are realized inside and outside the Bondi/SGI radius in M87 (Russell et al. 2015, 2018).

We further investigated the hot gas properties for other sources to check whether similar conditions to those in M87 could be established. However, the number of sources whose proximity to the central core can be spatially resolved by X-ray observations is limited, making it difficult to give accurate estimations of the Bondi radii for those sources. Therefore, we consider the SGI radius instead of the Bondi radius for the gravitational spheres of the central black holes. Note that we checked the temperature of the bright cores of several sources hosted by elliptical galaxies in our collected samples and confirmed that the Bondi radii are approximately of the same order of magnitude as the SGI radii[42] (e.g., Sun 2009; Fujita et al. 2016).

Here, the SGI radius is estimated as $R_{\rm SGI} = GM_{\rm BH}/\sigma_d^2 = (1/2)(c/\sigma_d)^2 R_s$, where σ_d is the stellar velocity dispersion. To investigate the relationship between the location of the SGI boundary and the jet collimation break among our samples with various BH masses, we introduced an empirical $M_{\rm BH}$–σ_d relation derived in Kormendy & Ho (2013). This relation is particularly strong for the classical bulge and elliptical galaxies, and our sample is supposed to follow this relation (e.g., see Table 2 in Kormendy & Ho 2013, and references therein). Indeed, 3C 273 follows the relation from the stellar velocity dispersion of $\sigma_d = 210\,{\rm km\,s^{-1}}$ (Husemann et al. 2019) and SMBH mass of $M_{\rm BH} = 2.6 \times 10^8\,M_\odot$, which gives us an estimation of the SGI radius as $R_{\rm SGI} \sim 10^6\,R_s$ (see the solid line in Figure 12).

The most important finding here is that the measured locations of the collimation breaks, including in 3C 273, are more widely distributed than the intrinsic scatter of the SGI locations seen in the samples of Kormendy & Ho (2013). In particular, NGC 4261 (Nakahara et al. 2018), NGC 1052 (Nakahara et al. 2020), and NGC 315 (Boccardi et al. 2021; Park et al. 2021) imply a transition of the jet collimation in a substantially more inner area than the SGI boundary. For NGC 315, Park et al. (2021) discussed that the nonrelativistic outflow, such as wind from the accretion disk, may play a critical role in jet collimation—for instance, the inner break of the jet collimation seen in NGC 315 may occur if the wind does not reach the Bondi radius or the edge of the SGI.

---

[42] Considering the empirical M–σ_d relation for an AGN with a typical black hole mass ($10^{8-9}\,M_\odot$), we expect the temperature of the hot gas in the central core to be ~0.1–1 keV when the Bondi radius is close to the SGI radius.

The other two sources have a common property at the jet base. They are surrounded by a dense obscuring disk/torus causing free–free absorption (FFA). For NGC 1052, the physical size of the FFA torus is $\sim$0.5 pc ($\sim 3.4 \times 10^4\, R_s$) in radius (Kameno et al. 2001), which is close to the deprojected break location of $\sim$0.15 pc reported by Nakahara et al. (2020).[43] For NGC 4261, Haga et al. (2015) estimated the transition radius in the accretion disk as $\sim 2 \times 10^3\, R_s$ from FFA measurements, which is close to the break in the jet shape at $\sim 10^4\, R_s$ for NGC 4261 (Nakahara et al. 2018).

The break location of 1H 0323+342 is not well constrained because of the significantly uncertain black hole mass. It shows a distant collimation break for the lower black hole mass (case B in Figure 12), while the jet collimation break occurs near the SGI for the larger black hole mass (case A). Hada et al. (2018) discussed that radiation-driven outflow/wind associated with the narrow-line region may confine the jet of 1H 0323 +342 (case B), while 1H 0323+342 and M87 may share the common jet collimation mechanism (case A), which is supported by 1H 0323+342 having a stationary recollimation shock at the transitional region like the HST-1 knot in M87 (see Doi et al. 2018).

Our results and Figure 12 indicate that the transition distance of the jet shape is not necessarily determined by the SGI boundary, but rather by its diverse environment, such as the presence of the disk, torus, or disk wind and their spatial extent. The hot gas cocoon surrounding the jet may also be an influence (e.g., Bromberg et al. 2011).

Recently, Boccardi et al. (2021) discussed the jet collimation properties of various radio galaxies with respect to the activity of the central accretion disk by categorizing samples into low- and high-excitation radio galaxies (LERGs and HERGs). They found that HERGs had larger radii and longer shape transition distances for the collimation properties. For 3C 273, it is unlikely that a component near the central engine, such as the torus, is the critical factor causing the break because the collimation break in the 3C 273 jet is outside the range of $\sim$100 pc. Then 3C 273, if viewed from a typical viewing angle of radio galaxies, would be categorized as a HERG given the high ratio of the X-ray luminosity L_X (2–10 keV) to the Eddington luminosity L_{Edd} implied by $L_X > 1.4 \times 10^{46}\, \mathrm{erg\, s^{-1}}$ (Cappi et al. 1998) and $L_{Edd} = 3.4 \times 10^{46}\, \mathrm{erg\, s^{-1}}$ given for $M_{BH} = 2.6 \times 10^8\, M_\odot$ (Gravity Collaboration et al. 2018). Therefore, our results for 3C 273, which show relatively large jet widths ($2r \gtrsim 10^4\, R_s$ at $z \gtrsim 10^5\, R_s$) and a distant location of the jet collimation break ($z_b > 10^6\, R_s$), are consistent with the statistical trend reported in Boccardi et al. (2021).

Finally, we briefly note a scenario in which the jet collimation break is governed by the internal jet physics proposed by Kovalev et al. (2020). They proposed that under a single ambient pressure profile, such as $p \propto z^{-2}$, the collimation break occurs in the region where the magnetic and particle energies are equivalent. In their model, the break location depends mainly on the initial magnetization parameters (σ_M) at the jet base, as well as on the black hole mass and spin (see Equation (7) in Nokhrina et al. 2020). The large σ_M for 3C 273 estimated in Nokhrina et al. (2015) may be qualitatively consistent with the distant jet collimation break found in this study. However, it is still hard to tightly constrain the value of σ_M, and this is still an open problem. Therefore, it remains unclear

whether this scenario can explain the diverse distributions of the break locations ranging from $10^4\, R_s$ to $10^8\, R_s$ shown in Figure 12. If the value of σ_M can be estimated accurately for more sources, the physical connection between σ_M and the break location could be discussed in more detail.

7. Summary

In this paper, we have investigated the global jet structure of the archetypical quasar 3C 273 with VLBA, HSA, and GMVA observations. In particular, we have reported on new GMVA observations at 86 GHz conducted in the first session involving ALMA, which significantly enhance the sensitivity and angular resolution of the images, providing the detailed morphology of the innermost jet. With the robust imaging analysis using the state-of-the-art RML imaging techniques, we obtained the jet collimation profile over a wide range of 10^5–$10^8\, R_s$ in deprojected distance. We summarize our results as follows.

1. The quasar 3C 273 jet is found to have the structural transition from semiparabolic to conical/hyperbolic shape at $\sim 10^7\, R_s$, providing the first clear example of a quasar jet. Our results suggest the existence of the jet collimation break for sources exhibiting widely different accretion rates.
2. The collimation break is located in the area at $\sim 4 \times 10^6$ to $10^7\, R_s$ where the jet shows a bending streamline for $\sim$10 mas that persists for more than the typical jet crossing time. The area is also known as the broadened vertical structure with two brightening limbs resolved by recent space-based VLBI observations. This peculiar and persistent feature, co-located with the jet break, may be explained by a stable magnetohydrodynamic feature, as HST-1 may be for M87.
3. The extrapolation of the collimation profile is consistent with the spatial distribution of BLRs and dusty winds resolved with recent GRAVITY observations. Our observations suggest that future higher-frequency observations, for instance with the Event Horizon Telescope at 230 and 345 GHz, can probe further inner regions where the jet might interact with such hot dusty ionized gas.
4. Comparison of the collimation profile of the 3C 273 jet with the velocity field obtained by long-term monitoring observations at 15 and 43 GHz shows that the 3C 273 jet is already accelerated to its apparent maximum velocity upstream of the collimation break, which is apparently different from the M87 jet, where the ends of the collimation and acceleration zones are co-located.
5. The collimation break of 3C 273 is located several to ten times further out than the estimated SGI location. Furthermore, we compared all available locations of the jet break from the literature with the SGI locations derived from the M_{BH}–σ_d relation, clearly showing that the transition of the jet collimation is governed not only by the SGI of the central black hole.
6. The relatively more distant location of the jet collimation break discovered for 3C 273 seems broadly consistent with the statistical trend of radio galaxies whereby higher-excitation AGN sources tend to end their jet collimation at more distant locations from the central black hole.

Our results demonstrate that ultrahigh-resolution observations with new millimeter facilities can provide many new

---

[43] The break location is consistent with an independent measurement by Kovalev et al. (2020) within a factor of $\sim$3.

insights into high-powered AGNs that were not previously suitable for study of their jet collimation. Further study using full polarimetric data and Faraday rotation synthesis can reveal the distribution of the three-dimensional magnetic field and the circumnuclear medium in the active collimation region (e.g., Park et al. 2019a). These explorations with polarimetric analysis using presented multifrequency data including GMVA +ALMA will be presented in a forthcoming paper.

Appendix
Model Selection

We describe the model selection for our fitting analysis to the jet radius profile presented in Section 5.5. To choose a better model to explain the overall jet structure, we performed a fitting analysis using single and broken power-law functions for entire measurements except for the rapid increase in jet radii around $\sim 10^7\,R_s$ (see Section 5.5). Then we checked their fractional deviations δ defined as

$$\delta = \frac{r - r_{\mathrm{model}}}{r_{\mathrm{model}}}. \tag{A1}$$

For the case of a single power-law fit in Figure 13, the deviations from the model are seen at both inner and outer edges, while they are relatively small for a broken power-law fit.

For more quantitative comparison, we computed the normalized mean square error (NRMSE) values (e.g., Chael et al. 2016; Akiyama et al. 2017a, 2017b) for each model, defined as

$$\mathrm{NRMSE} = \sqrt{\frac{\Sigma(r - r_{\mathrm{model}})^2}{\Sigma r_{\mathrm{model}}^2}}. \tag{A2}$$

As shown in Figure 13, the resultant NRMSE value for the broken power-law model is lower than that for the single power-law model, also suggesting that the broken power-law function is a better model for describing the whole range of measured jet radii of 3C 273.
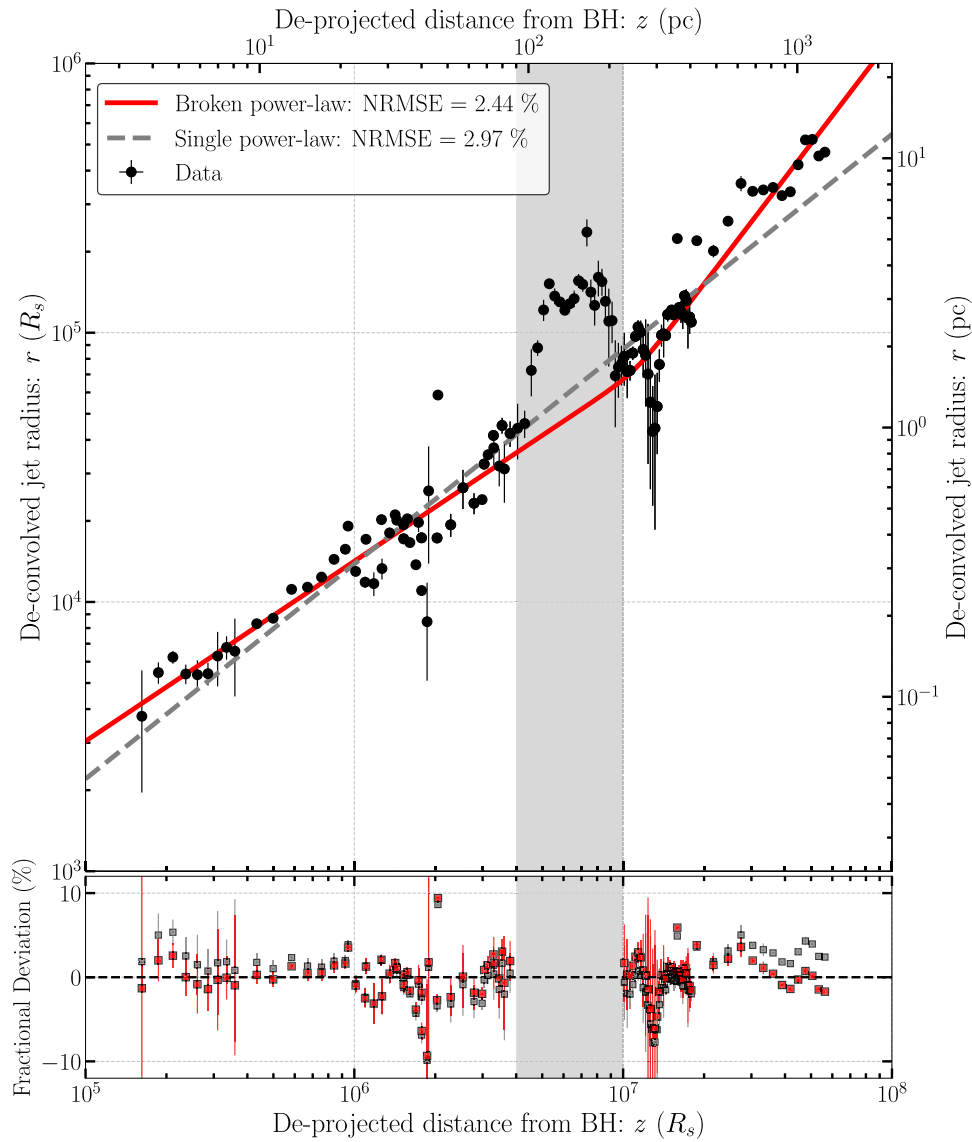
Figure 13. Upper panel: radial profile of the jet in 3C 273 with different models of power-law functions. Measurement data are the same as in Figure 8. The gray dashed line shows the best-fit single power-law function ($r \propto z^a$) with $a = 0.80$ obtained from all the data except for the gray shaded region. The red solid line shows the best-fit broken power-law function as presented in Figure 8. Lower panel: fractional deviations of the jet radii from the obtained models. The red and gray squares correspond to the deviations from the lines in the upper panel.

ORCID iDs

Hiroki Okino ⓘ https://orcid.org/0000-0003-3779-2016
Kazunori Akiyama ⓘ https://orcid.org/0000-0002-9475-4254
Keiichi Asada ⓘ https://orcid.org/0000-0001-6988-8763
José L. Gómez ⓘ https://orcid.org/0000-0003-4190-7613
Kazuhiro Hada ⓘ https://orcid.org/0000-0001-6906-772X
Mareki Honma ⓘ https://orcid.org/0000-0003-4058-9000
Thomas P. Krichbaum ⓘ https://orcid.org/0000-0002-4892-9586
Motoki Kino ⓘ https://orcid.org/0000-0002-2709-7338
Hiroshi Nagai ⓘ https://orcid.org/0000-0003-0292-3645
Uwe Bach ⓘ https://orcid.org/0000-0002-7722-8412
Lindy Blackburn ⓘ https://orcid.org/0000-0002-9030-642X
Katherine L. Bouman ⓘ https://orcid.org/0000-0003-0077-4367
Andrew Chael ⓘ https://orcid.org/0000-0003-2966-6220
Geoffrey B. Crew ⓘ https://orcid.org/0000-0002-2079-3189
Sheperd S. Doeleman ⓘ https://orcid.org/0000-0002-9031-0904

Vincent L. Fish ⓘ https://orcid.org/0000-0002-7128-9345
Ciriaco Goddi ⓘ https://orcid.org/0000-0002-2542-7743
Sara Issaoun ⓘ https://orcid.org/0000-0002-5297-921X
Michael D. Johnson ⓘ https://orcid.org/0000-0002-4120-3029
Svetlana Jorstad ⓘ https://orcid.org/0000-0001-6158-1708
Shoko Koyama ⓘ https://orcid.org/0000-0002-3723-3372
Colin J. Lonsdale ⓘ https://orcid.org/0000-0003-4062-4654
Ru-Sen Lu ⓘ https://orcid.org/0000-0002-7692-7967
Ivan Martí-Vidal ⓘ https://orcid.org/0000-0003-3708-9611
Lynn D. Matthews ⓘ https://orcid.org/0000-0002-3728-8082
Yosuke Mizuno ⓘ https://orcid.org/0000-0002-8131-6730
Kotaro Moriyama ⓘ https://orcid.org/0000-0003-1364-3761
Masanori Nakamura ⓘ https://orcid.org/0000-0001-6081-2420
Hung-Yi Pu ⓘ https://orcid.org/0000-0001-9270-8812
Eduardo Ros ⓘ https://orcid.org/0000-0001-9503-4892
Tuomas Savolainen ⓘ https://orcid.org/0000-0001-6214-1085
Fumie Tazaki ⓘ https://orcid.org/0000-0003-0236-0600

Jan Wagner ⬤ https://orcid.org/0000-0003-1105-6109
Maciek Wielgus ⬤ https://orcid.org/0000-0002-8635-4242
Anton Zensus ⬤ https://orcid.org/0000-0001-7470-3321

References

Agudo, I., Thum, C., Molina, S. N., et al. 2018, MNRAS, 474, 1427
Akiyama, K., Asada, K., Fish, V., et al. 2018, Galax, 6, 15
Akiyama, K., Ikeda, S., Pleau, M., et al. 2017a, AJ, 153, 159
Akiyama, K., Kuramochi, K., Ikeda, S., et al. 2017b, ApJ, 838, 1
Algaba, J. C., Nakamura, M., Asada, K., & Lee, S. S. 2017, ApJ, 834, 65
Algaba, J. C., Rani, B., Lee, S. S., et al. 2019, ApJ, 886, 85
Angelakis, E., Fuhrmann, L., Marchili, N., et al. 2015, A&A, 575, A55
Asada, K., & Nakamura, M. 2012, ApJL, 745, L28
Asada, K., Nakamura, M., Doi, A., Nagai, H., & Inoue, M. 2014, ApJL, 781, L2
Astropy Collaboration, Price-Whelan, A. M., Sipőcz, B. M., et al. 2018, AJ, 156, 123
Astropy Collaboration, Robitaille, T. P., Tollerud, E. J., et al. 2013, A&A, 558, A33
Baczko, A. K., Ros, E., Kadler, M., et al. 2022, A&A, 658, A119
Bahcall, J. N., Kirhakos, S., Schneider, D. P., et al. 1995, ApJL, 452, L91
Begelman, M. C., & Li, Z.-Y. 1994, ApJ, 426, 269
Blackburn, L., Pesce, D. W., Johnson, M. D., et al. 2020, ApJ, 894, 31
Blandford, R., Meier, D., & Readhead, A. 2019, ARA&A, 57, 467
Blandford, R. D., & Königl, A. 1979, ApJ, 232, 34
Boccardi, B., Krichbaum, T. P., Bach, U., Bremer, M., & Zensus, J. A. 2016, A&A, 588, L9
Boccardi, B., Krichbaum, T. P., Ros, E., & Zensus, J. A. 2017, A&ARv, 25, 4
Boccardi, B., Migliori, G., Grandi, P., et al. 2019, A&A, 627, A89
Boccardi, B., Perucho, M., Casadio, C., et al. 2021, A&A, 647, A67
Bromberg, O., Nakar, E., Piran, T., & Sari, R. 2011, ApJ, 740, 100
Bruni, G., Gómez, J. L., Casadio, C., et al. 2017, A&A, 604, A111
Bruni, G., Gómez, J. L., Vega-García, L., et al. 2021, A&A, 654, A27
Cappi, M., Matsuoka, M., Otani, C., & Leighly, K. M. 1998, PASJ, 50, 213
Chael, A., Rowan, M., Narayan, R., Johnson, M., & Sironi, L. 2018, MNRAS, 478, 5209
Chael, A. A., Johnson, M. D., Narayan, R., et al. 2016, ApJ, 829, 11
Conway, R. G., Garrington, S. T., Perley, R. A., & Biretta, J. A. 1993, A&A, 267, 347
Croke, S. M., & Gabuzda, D. C. 2008, MNRAS, 386, 619
Davis, R. J., Muxlow, T. W. B., & Conway, R. G. 1985, Natur, 318, 343
Deller, A. T., Brisken, W. F., Phillips, C. J., et al. 2011, PASP, 123, 275
Deller, A. T., Tingay, S. J., Bailes, M., & West, C. 2007, PASP, 119, 318
Doi, A., Hada, K., Kino, M., Wajima, K., & Nakahara, S. 2018, ApJL, 857, L6
Event Horizon Telescope Collaboration, Akiyama, K., Alberdi, A., et al. 2019a, ApJL, 875, L1
Event Horizon Telescope Collaboration, Akiyama, K., Alberdi, A., et al. 2019b, ApJL, 875, L4
Fromm, C. M., Perucho, M., Porth, O., et al. 2018, A&A, 609, A80
Fromm, C. M., Ros, E., Perucho, M., et al. 2013, A&A, 557, A105
Fromm, C. M., Younsi, Z., Baczko, A., et al. 2019, A&A, 629, A4
Fuhrmann, L., Angelakis, E., Zensus, J. A., et al. 2016, A&A, 596, A45
Fujita, Y., Kawakatu, N., & Shlosman, I. 2016, PASJ, 68, 26
Giovannini, G., Savolainen, T., Orienti, M., et al. 2018, NatAs, 2, 472
Goddi, C., Martí-Vidal, I., Messias, H., et al. 2019, PASP, 131, 075003
Gómez, J. L., Lobanov, A. P., Bruni, G., et al. 2016, ApJ, 817, 96
Gravity Collaboration, Sturm, E., Dexter, J., et al. 2018, Natur, 563, 657
Gravity Collaboration, Dexter, J., Shangguan, J., et al. 2020, A&A, 635, A92
Gravity Collaboration, Abuter, R., Accardo, M., et al. 2017, A&A, 602, A94
Greisen, E. W. 2003, in AIPS, the VLA, and the VLBA, Astrophysics and Space Science Library, ed. A. Heck, Vol. 285 (Dordrecht: Kluwer), 109
Hada, K. 2019, Galax, 8, 1
Hada, K., Doi, A., Kino, M., et al. 2011, Natur, 477, 185
Hada, K., Doi, A., Wajima, K., et al. 2018, ApJ, 860, 141
Hada, K., Kino, M., Doi, A., et al. 2013, ApJ, 775, 70
Hada, K., Kino, M., Doi, A., et al. 2016, ApJ, 817, 131
Haga, T., Doi, A., Murata, Y., et al. 2015, ApJ, 807, 15
Högbom, J. A. 1974, A&AS, 15, 417
Homan, D. C., Lister, M. L., Kovalev, Y. Y., et al. 2015, ApJ, 798, 134
Honma, M., Akiyama, K., Uemura, M., & Ikeda, S. 2014, PASJ, 66, 95
Hovatta, T., Aller, M. F., Aller, H. D., et al. 2014, AJ, 147, 143
Hunter, J. D. 2007, CSE, 9, 90
Husemann, B., Bennert, V. N., Jahnke, K., et al. 2019, ApJ, 879, 75
Ikeda, S., Tazaki, F., Akiyama, K., Hada, K., & Honma, M. 2016, PASJ, 68, 45

Issaoun, S., Johnson, M. D., Blackburn, L., et al. 2019, ApJ, 871, 30
Janssen, M., Falcke, H., Kadler, M., et al. 2021, NatAs, 5, 1017
Jester, S., Röser, H.-J., Meisenheimer, K., & Perley, R. 2005, A&A, 431, 477
Jorstad, S. G., Marscher, A. P., Lister, M. L., et al. 2005, AJ, 130, 1418
Jorstad, S. G., Marscher, A. P., Morozova, D. A., et al. 2017, ApJ, 846, 98
Kameno, S., Sawada-Satoh, S., Inoue, M., Shen, Z.-Q., & Wajima, K. 2001, PASJ, 53, 169
Kim, J.-Y., Krichbaum, T. P. & Event Horizon Telescope Collaboration 2020, A&A, 640, A69
Kim, J.-Y., Krichbaum, T. P., Lu, R.-S., et al. 2018, A&A, 616, A188
Komissarov, S. S., Barkov, M. V., Vlahakis, N., & Königl, A. 2007, MNRAS, 380, 51
Komissarov, S. S., Vlahakis, N., Königl, A., & Barkov, M. V. 2009, MNRAS, 394, 1182
Kormendy, J., & Ho, L. C. 2013, ARA&A, 51, 511
Kovalev, Y. Y., Kardashev, N. S., Kellermann, K. I., et al. 2016, ApJL, 820, L9
Kovalev, Y. Y., Pushkarev, A. B., Nokhrina, E. E., et al. 2020, MNRAS, 495, 3576
Koyama, S., Kino, M., Giroletti, M., et al. 2016, A&A, 586, A113
Krichbaum, T. P., Witzel, A., Booth, R. S., et al. 1990, A&A, 237, 3
Kuramochi, K., Akiyama, K., Ikeda, S., et al. 2018, ApJ, 858, 56
Li, Y.-R., Wang, J.-M., Songsheng, Y.-Y., et al. 2022, ApJ, 927, 58
Lisakov, M. M., Kovalev, Y. Y., Savolainen, T., Hovatta, T., & Kutkin, A. M. 2017, MNRAS, 468, 4478
Lister, M. L., Aller, M. F., Aller, H. D., et al. 2018, ApJS, 234, 12
Lister, M. L., Homan, D. C., Hovatta, T., et al. 2019, ApJ, 874, 43
Lister, M. L., Homan, D. C., Kellermann, K. I., et al. 2021, ApJ, 923, 30
Lobanov, A. P. 1998, A&A, 330, 79
Lobanov, A. P., & Zensus, J. A. 2001, Sci, 294, 128
Matthews, L. D., Crew, G. B., Doeleman, S. S., et al. 2018, PASP, 130, 015002
McKinney, W. 2010, in Proc. of the 9th Python in Science Conf., ed. S. van der Walt & J. Millman (Austin: SciPy), 56
Mertens, F., & Lobanov, A. 2015, A&A, 574, A67
Meyer, E. T., Sparks, W. B., Georganopoulos, M., et al. 2016, ApJ, 818, 195
Mizuno, Y., Gómez, J. L., Nishikawa, K.-I., et al. 2015, ApJ, 809, 38
Nagai, H., Haga, T., Giovannini, G., et al. 2014, ApJ, 785, 53
Nakahara, S., Doi, A., Murata, Y., et al. 2018, ApJ, 854, 148
Nakahara, S., Doi, A., Murata, Y., et al. 2019, ApJ, 878, 61
Nakahara, S., Doi, A., Murata, Y., et al. 2020, AJ, 159, 14
Nakamura, M., & Asada, K. 2013, ApJ, 775, 118
Nakamura, M., Asada, K., Hada, K., et al. 2018, ApJ, 868, 146
Nokhrina, E. E., Beskin, V. S., Kovalev, Y. Y., & Zheltoukhov, A. A. 2015, MNRAS, 447, 2726
Nokhrina, E. E., Kovalev, Y. Y., & Pushkarev, A. B. 2020, MNRAS, 498, 2532
O'Sullivan, S. P., & Gabuzda, D. C. 2009, MNRAS, 400, 26
Park, J., Hada, K., Kino, M., et al. 2019a, ApJ, 871, 257
Park, J., Hada, K., Kino, M., et al. 2019b, ApJ, 887, 147
Park, J., Hada, K., Nakamura, M., et al. 2021, ApJ, 909, 76
Perley, R. A., & Meisenheimer, K. 2017, A&A, 601, A35
Planck Collaboration, Ade, P. A. R., Aghanim, N., et al. 2014, A&A, 571, A16
Pushkarev, A. B., Hovatta, T., Kovalev, Y. Y., et al. 2012, A&A, 545, A113
Pushkarev, A. B., Kovalev, Y. Y., Lister, M. L., & Savolainen, T. 2017, MNRAS, 468, 4992
Russell, H. R., Fabian, A. C., McNamara, B. R., et al. 2018, MNRAS, 477, 3583
Russell, H. R., Fabian, A. C., McNamara, B. R., & Broderick, A. E. 2015, MNRAS, 451, 588
Savolainen, T., Wiik, K., Valtaoja, E., & Tornikoski, M. 2006, A&A, 446, 71
Schmidt, M. 1963, Natur, 197, 1040
Shepherd, M. C. 1997, in ASP Conf. Ser. 125, Astronomical Data Analysis Software and Systems VI, ed. G. Hunt & H. Payne (San Francisco, CA: ASP), 77
Sun, M. 2009, ApJ, 704, 1586
Thompson, A. R., Moran, J. M., & Swenson, G. W., Jr. 2017, Interferometry and Synthesis in Radio Astronomy (3rd ed.; Berlin: Springer)
Tseng, C.-Y., Asada, K., Nakamura, M., et al. 2016, ApJ, 833, 288
van der Walt, S., Colbert, S. C., & Varoquaux, G. 2011, CSE, 13, 22
Virtanen, P., Gommers, R., Oliphant, T. E., et al. 2020, NatMe, 17, 261
Walker, R. C., Hardee, P. E., Davies, F. B., Ly, C., & Junor, W. 2018, ApJ, 855, 128
Yamaguchi, M., Akiyama, K., Tsukagoshi, T., et al. 2020, ApJ, 895, 84
Zhao, G.-Y., Gómez, J. L., Fuentes, A., et al. 2022, ApJ, 932, 72